

***Politecnico
di Torino***

Dipartimento di Elettronica e
Telecomunicazioni (DET)



Laurea Magistrale in Ingegneria
Telematica e delle Comunicazioni

***Universidad Politécnica
de Madrid***

Departamento de Tecnología Fotónica
y Bioingeniería (TFB)



Máster Universitario en Ingeniería de
Telecomunicación

Master Thesis

**Design, Simulation, Manufacturing and
Characterization of a tunable Beam Steering
device based on Liquid Crystals**

Supervisors

Dr. Morten Andreas Geday

Dr. Guido Perrone

Mr. Mario García de Blas

Author

Sergio Vera Andreu

July 2021

Abstract

In this project a new high performing 2D beam deflector with no movable parts will be developed. The device will be composed by two cascaded liquid crystal cells, each one steering the beam in one dimension. The active area of the device will be $1.08 \times 1.08 \text{ mm}^2$. The cells will be composed by 144 electrodes with $7.5 \text{ }\mu\text{m}$ pitch width, driven by a custom made 12-bit Pulse Width Modulation (PWM) electronical driver. Direct Laser Writing (DLW) techniques will be employed to obtain high-resolution structures, with a high fill factor, in glass wafers coated with Indium-Tin Oxide (ITO). A 144×144 efficiency map will be presented, for a maximum diagonal steering angle of $\pm 3,42^\circ$. The results will be accompanied by a simulation based on Fresnel and Fraunhofer diffraction approximation.

Keywords

LC-OPA, Beam Steering, Liquid Crystal, Free Space Communications, Blaze Grating, Direct Laser Writing.

Acknowledgements

To all the people from CEMDATIC; specially to Morten, the responsible for enrolling me into a world that I would not have known in any other way just with a couple of jokes about light sabers, and Mario, that had to be my nanny during all this process.

Thanks to you this has become the most pleasurable stage of my whole academic career.

Index

1. INTRODUCTION	1
1.1. THESIS STRUCTURE AND OBJECTIVES	1
2. STATE OF ART	3
2.1. LIQUID CRYSTALS	3
2.2. BEAM STEERERS	4
3. THEORETICAL BACKGROUND	8
3.1. BIREFRINGENCE	8
3.2. LIQUID CRYSTALS	10
3.3. LIQUID CRYSTAL OPTICALLY PHASED ARRAYS	10
3.4. DEVICE SUMMARY	12
4. DEVICE DESIGN	14
4.1. LC CELLS	14
4.2. ELECTRONIC DRIVER	17
5. MANUFACTURING	18
5.1. STEPS TO MANUFACTURE THE LC-OPA CELL	18
5.2. COMMON ISSUES	29
6. CHARACTERIZATION	31
6.1. SET-UP	31
6.2. RESULTS	32
7. SIMULATION	35
7.1. THEORETICAL BACKGROUND	35
7.2. DEVICE MODEL	37
7.3. DIFFRACTION EFFICIENCY	38
7.4. STEERING ANGLE	43
8. RESULTS	46
8.1. PROCEDURE	46
8.2. 1D DEVICE RESULTS	46
8.3. 2D DEVICE RESULTS.	49
9. CONCLUSIONS	52
9.1. FUTURE LINES	52
10. ANNEX	53
10.1. ETHICAL, ECONOMIC, SOCIAL, AND ENVIRONMENTAL ASPECTS	53
10.2. ECONOMIC BUDGET	55
10.3. LABVIEW ROUTINES	57
10.4. MATLAB ROUTINES	60
11. BIBLIOGRAPHY	74

Figure index

Figure 1: Basic structure of a LCD.....	3
Figure 2: LC used as thermometer	4
Figure 3: LC used as smart glass	4
Figure 4: Newport FSM – Model FSM-300-01 13.....	5
Figure 5: Aerotech gimbal - Model AMG100GR.....	5
Figure 6: Kim et al. beam steering device	7
Figure 7: Refractive index ellipsoid	9
Figure 8: Nematic phase.....	10
Figure 9: Equivalent Fresnel lens.	11
Figure 10: Concept of a LC OPA.....	11
Figure 11: Phase modulation of LC-OPA	12
Figure 12: VBG scheme with 12 pixels.	13
Figure 13: Diagram of a LC-OPA cell.....	14
Figure 14: CAD complete design	15
Figure 15: Details from CAD design.....	17
Figure 16: Electronic driver.	17
Figure 17: Wafer cutting process.....	18
Figure 18: CEMDATIC clean room laser.....	19
Figure 19: Clean room laser - optical setup.	20
Figure 20: AFM image (a) and measured profile (b) for upper and bottom ablation.....	21
Figure 21: Jetlight UVO-Cleaner® model 18.....	22
Figure 22: Lab rotatory disk.	23
Figure 23: Lab hotplate.	23
Figure 24: Lab roller.	24
Figure 25: Effect of rubbing at LC orientation.....	24
Figure 26: Ultrasounds bath machine.....	25
Figure 27: Cell gluing	26
Figure 28: Vacuum bell.....	26
Figure 29: Thermal press.....	27
Figure 30: 1D device – “Sample 3”.....	28
Figure 31: Cell alignment during 2D device assembly.....	28
Figure 32: 2D device - “Sample 5” and “Sample 7”	29
Figure 33: “Sample 1” (a) and “Sample 3” (b) microscope caption when using a Topology +2.	30
Figure 34: Characterization set-up.....	31
Figure 35: Characterization charts. (a) “Sample 5”, (b) “Sample 7”.	33
Figure 36: Measured intensity vs fitted intensity. (a) “Sample 5”, (b) “Sample 7”	34
Figure 37: Diffraction geometry.....	35
Figure 38: Electrodes model. Example for fill ratio of 5/6.	37
Figure 39: Electrodes phase distribution in an ideal case and the modelled VBG schemes.....	38
Figure 40: Diffraction pattern for topology (+12,+12)	40
Figure 41: 2D grating efficiency for complete device (2 cells).	41
Figure 42: Grating efficiency (2 cells) contour.	42
Figure 43: Grating efficiency (2 cells) cuts.	42
Figure 44: Angle of deflection simulated and calculated analytically.....	43
Figure 45: Deviation angle map.	44
Figure 46: Diffraction efficiency as a function of the angle of deflection.....	45

Figure 47: Results set-up.....	46
Figure 48: Steered beam with "Sample 5"	48
Figure 49: 2D Steered beam with "Sample 5" and "Sample 7"	51

Table index

Table 1: Model parameters for “Sample 5” and “Sample 7”	33
Table 2: 1D and 2D device results.	51

Abbreviations

ACA	<i>Anisotropic Conductive Adhesive</i>
CAD	<i>Computer Assisted Design</i>
CNC	<i>Computer Numerical Control</i>
ITO	<i>Indium Tin Oxide</i>
LC	<i>Liquid Crystal</i>
LCD	<i>Liquid Crystal Display</i>
LC-OPA	<i>Liquid Crystal – Optical Phased Array</i>
LIDAR	<i>Laser Imaging Detection and Ranging</i>
MEMS	<i>Microelectromechanical Systems</i>
PCB	<i>Printed Circuit Board</i>
PLA	<i>Polylactic Acid</i>
PVP	<i>Polyvinylpyrrolidone</i>
PWM	<i>Pulse Width Modulation</i>
SWaP	<i>Size, Weight and Power</i>
VBG	<i>Variable Blazing Grating</i>
VPG	<i>Variable Period Grating</i>

1. Introduction

Changing the direction of a light beam is a trivial necessity for many applications, such as free space communications⁸, optical tweezers⁷, and Light, Detection and Ranging (LIDAR) devices⁹.

As technology advances, more refined beam steerers have been developed¹². From more artisanal approaches such as building reflecting mirror schemes, to current designs based on microelectromechanical systems (MEMS), among many others; the approaches have varied along time.

This paper will focus on optical phased arrays. Advances in liquid crystals and improved manufacturing processes have opened a new stream of non-mechanical devices with potential advantages in terms of Size, Weight and Power (SWaP) over current devices.

Within this framework, a design for the manufacture of a low-cost beam steering device will be proposed and its performance will be studied with respect to other current options in the market.

1.1. Thesis structure and objectives

This Master Thesis will investigate the current state of Liquid Crystal Optical Phased Arrays (LC-OPA) for Beam Steering, to develop an operative device that exhibit the expected behavior. The study will be accompanied by theoretical simulations complementing the measures obtained.

After an introduction about the topic, the current trends for beam steering devices are presented in **Chapter 2**. A distinction between devices based on mechanical and non-mechanical systems will be made to emphasize our device advantages.

In **Chapter 3** the theoretical topics will be discussed, hereunder light polarization and birefringence. Subsequently the type of liquid crystals that will be employed for the device manufacturing will be presented, as well as the optical phased array scheme that will be implemented.

Chapter 4 will contain the design of the device. *I.e.* the different layers in the Liquid Crystal (LC) cell. Then, the pixelated layer will be discussed.

In the manufacturing section, **Chapter 5**, the manufacture process will be segmented. Special attention will be given to the materials employed and the instrumentation used.

In **Chapter 6**, characterization of the manufactured cells is presented. The relation between the induced phase delay and input voltage will be shown. A pseudo exponential function will be implemented to fit the curve and follow the behavior of the cells with an analytical model instead than with an experimental one.

Chapter 7 will show the simulations made to compare the measured results with the theoretical ones. A theoretical introduction to explain the outcome of the diffraction patterns will be made. In addition, a realistic model to describe the electrodes structure and the influence of crosstalk, fringe effects, fill-ratio, *etc.* will be presented.

Chapter 8 will present data about the real device performance, in terms of diffraction efficiency and angle of deflection. The measured results will be accompanied by comments comparing them with the simulation results.

Finally, **Chapter 9** will include the thesis conclusions. The results will be compared with the initial design objectives. A 'Future lines' section will be included, where it will be tried to discern what could be done to improve this work.

2. State of art

Along this section, a brief summary about the current applications for Liquid Crystals will be derived. In addition to this, the trends for beam steering applications will be analyzed, and the devices that fulfill the market currently will be noted.

2.1. Liquid Crystals

Liquid crystals are a key component of many current technological devices. Its particular physical properties, being an intermediate phase between solids and liquids, are specially interesting in an optical sense.

The main application for this material is Liquid Crystal Displays (LCD). Having the ability to change the orientation of its optical birefringence applying an electric field to its molecules, a device that allows the change of light polarization as desired can be built.

Mounting a couple of orthogonal polarizers at the input and output of the liquid crystal layer will allow or impede the light cross the device, creating a barrier for the displays that could get transparent or opaque on command. A possible scheme is shown at Figure 1.

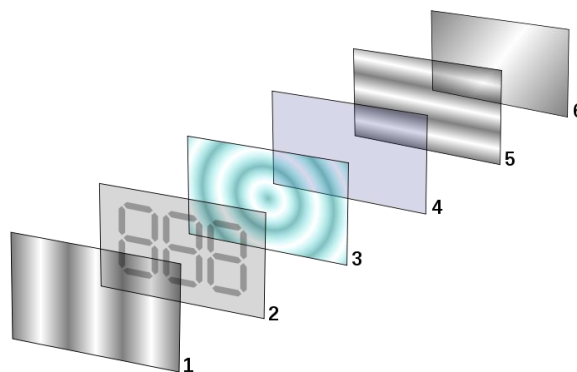


Figure 1: Basic structure of a LCD. (1) Vertical polarizer, (2) Patterned ITO layer, (3) LC, (4) ITO layer, (5) Horizontal polarizer, (6) Light reflector¹

Applications may use LCs as light filters to modify light properties in several ways. LCs may be found in electrooptical devices, as lenses² or lasers³, using them as tunable filters or modifying the optical path followed by light. One of the applications inside the electrooptical devices is beam steering. This will be further developed in the following subsection.

Other uses that could be given to LCs are:

1. **Thermometers.** Some kinds of LCs (thermochromic) modify its characteristics with temperature. It can alter the color seen, becoming quite useful for temperature measurements.⁴

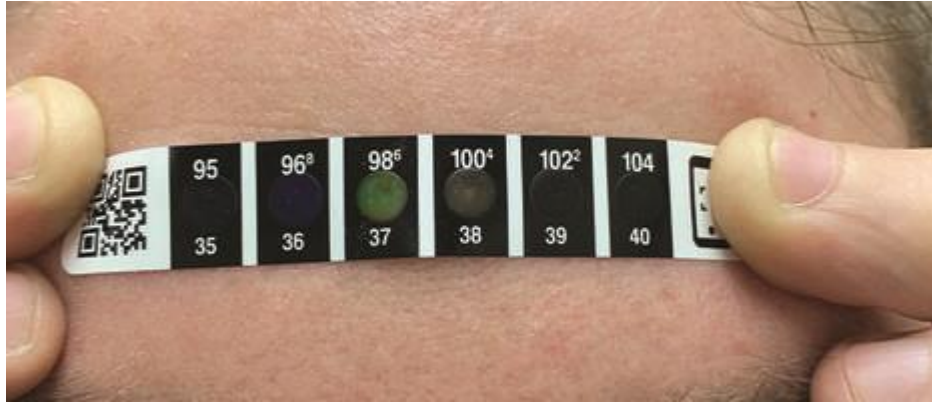


Figure 2: LC used as thermometer ⁵.

2. **Smart glasses.** As explained above for a LCD, the transparency of a glass could be modified simply at buildings or vehicles, eliminating the need of blinds, shades, or window treatments.

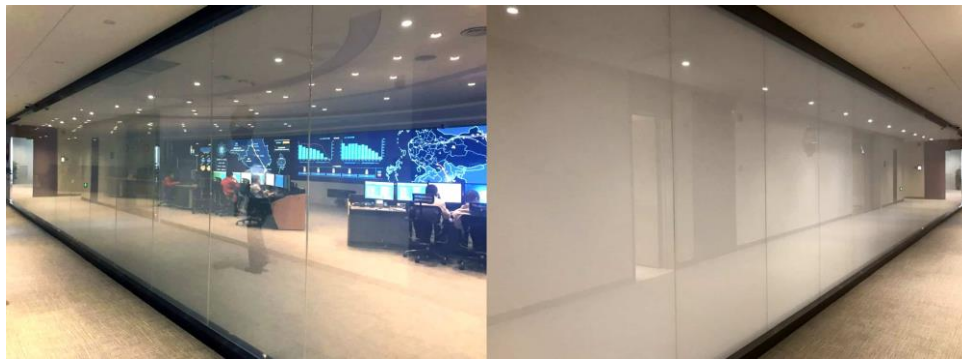


Figure 3: LC used as smart glass ⁶.

2.2. Beam steerers

There are numerous applications where a beam steerer is a key component. Optical tweezers⁷, free-space communications ⁸, LIDAR^{9,10,11} are some of the areas where it is needed. Beam steerers allow to change the direction of propagation of an electromagnetic beam using different techniques. A first division could be made into mechanical and non-mechanical approaches¹².

Mechanical systems are the ones used for most applications. Some of the main ones are:

1. **Gimbals.** They are the choice for high performance systems. Common in military applications and long distance commercial sensors.
2. **Fast Steering Mirrors.** Fast, reliable, and cheap, they are the ones that must be beaten by non-mechanical systems for short range or low-cost applications. As its size are small, it is needed to magnify the beam afterwards, which being the steered angle inversely proportional to the magnification turns into a handicap.
3. **Risley Prisms.** Its working principle is simply the rotation of its components. They can work with moderate size beams.
4. **Lenslet Arrays and MEMs.** They make use of micro-motion movements. Although they show problems to be stable in dynamic environments, they are reasonable fast and inexpensive. Its main disadvantage is that they need for continuous adjustments to maintain alignment, being therefore sensitive to noise.

Mechanical systems are more sensible to physical phenomena like inertia. In applications like free-space communications, this is especially relevant. It could be seen a trend into substituting these mechanical systems with non -mechanical devices that are more robust for harsh environments.

An example of a commercial device, to compare the values with the device that will be presented ahead, is the model FSM-300-01 from Newport¹³. With an angular range of $\pm 1.5^\circ$, a reflectivity $>93\%$ for the visible spectrum and an accuracy of $0,015^\circ$ rms; the performance is outstanding. The main drawbacks are the operative temperature range and the weight, which could turn quite problematic depending on the situation, always taking into account that this is not the objective of this device.



Figure 4: Newport FSM – Model FSM-300-01 ¹³.

On the other hand, to present a high-performance device, the gimbal AMG100GR from Aerotech¹⁴ gets an accuracy of $0,0033^\circ$, with a continuous angular range. The datasheet does not show the quality of the reflector for the built-in option.



Figure 5: Aerotech gimbal - Model AMG100GR ¹⁴.

Non-mechanical systems avoid any movable component to obtain the beam steering. Two approaches are being used: dynamically creating an optical path difference, which will generate a phase change at a particular wavelength; or creating a phase difference, that is equivalent to a certain optical path difference at a given wavelength. Some relevant approaches are¹⁵:

1. **Electro-optic devices.** Suitable for high speed, high throughput, low power, and low deflection angles; these devices using bulk crystals are larger, heavier and require higher driving voltages than the mechanical systems presented above.
2. **Acousto-optic cells.** They are quite fast and appropriate for deflecting beams in one direction, although the deflection angles, to stay in a reasonable efficiency margin, are not large. They are relatively expensive and difficult to mass produce.
3. **Liquid crystal devices.** Low-cost and low driving voltages are the main characteristics of these devices. Nematic LC presents a moderate switching speed, but it could be solved by using ferroelectric LC at a cost on the efficiency. They constitute a competitive alternative to MEMs switches when used as diffractive gratings for spatial light modulators.

Due to the reasons commented above, LCs constitute a good choice when the operation requirements need simple electronic drivers, small sizes, low weight, low power, and low cost. In addition to this, it is especially relevant the fact that avoiding the use of mechanical parts, the costs of maintenance drops. This is quite important when used for space applications¹⁶.

Some of the solutions implemented are optical phased arrays, compound blazed gratings, resistive electrodes, LC-cladding waveguides, Pancharatnam-Berry phase gratings, and volume gratings. A recent review of these solutions can be found at reference 17, where the operation principles of each approach are discussed, as well as some key parameters of performance.

Related to the devices that will be developed in this work, optical phased arrays based on liquid crystals for free-space commutation, could be pointed out the work from Kim et al. (2020)¹⁸. The optical phased arrays discussed in this work are passive. This is, the beam is formed previously and deflected when entering at the steering device instead of active approaches where individual transmit modules form the beam for a given direction directly.

The beam deflector manufactured in this work counts with 7200 controllable channels in an active area, or diffraction zone, of 14,4 x 14,4 mm²; obtaining a steering angle of 7,6°, with an angular resolution or minimum angular step of 0,021°, at a wavelength of 532 nm. The experimental measure for a diffraction efficiency of 50% leads to a maximum angle of around 1°; which again put in evidence the limitation of these kind of devices when low losses are needed for high deflection angles. The electrode pitch elected is 2 µm, with an interpixel length of 0,5 µm. The thickness of the LC layer is 2,5 µm. An image of the discussed device will be presented at Figure 6.

In this work the terms “pixel” and “electrode” will be employed to refer to the conductive zone at the ITO layer that will polarize the LC in discrete zones. The zone where the ITO has been removed, is called “interpixel”.

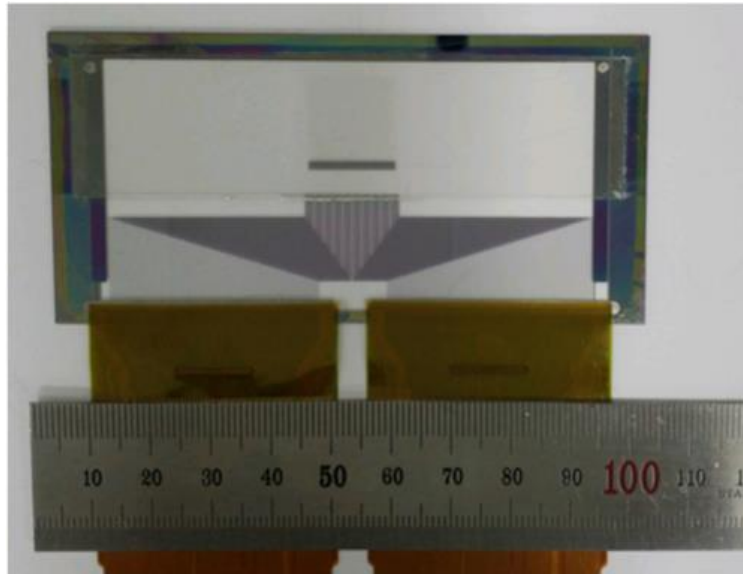


Figure 6: Kim et al. beam steering device ¹⁸.

Regarding the operation of the device, one of the main difficulties resides in the trade-off relation between the active area size and the steering angle obtained. Being a constraint the number of control electrodes available to emulate the phase profiles, a reduction of the pitch will directly mean smaller apertures. The interest in the reduction of the pitch (ideally) is due to obtaining steeper profiles in the same space.

The manufactured device in this work will try to increase the functionality of this kind of devices. Most of the beam steering devices presented at bibliography have operation principles that limit them to one dimension steering. It will compete, with the reference devices in the LC-OPA field extending the available dimensions to two. The expected outcome is a device with high fill-factor that obtains good angle diffraction ranges with simple electronic drivers.

3. Theoretical Background

To facilitate the understanding of the following chapters, a quick theoretical introduction will be presented in this segment; presenting the physical phenomena from which we take advantage, the material to which it applies, and the relevancy to the operation of the device.

3.1. Birefringence

In certain cases, the propagation and polarization of light might be affected by the internal structure of the material. The light will experience different refractive index depending on the alignment of the electric field. This optical property is known as **birefringence**, and these (optically) anisotropic materials are said to be birefringent¹⁹.

Asymmetries in the crystal lattice, or organization of its inner structure, can cause the medium polarization to respond in a different direction than the electric field ($P \neq \epsilon_0 \chi E$). The relation between these physical properties in a general form is:

$$\begin{bmatrix} P_x \\ P_y \\ P_z \end{bmatrix} = \epsilon_0 \begin{bmatrix} \chi_{xx} & \chi_{xy} & \chi_{xz} \\ \chi_{yx} & \chi_{yy} & \chi_{yz} \\ \chi_{zx} & \chi_{zy} & \chi_{zz} \end{bmatrix} \begin{bmatrix} E_x \\ E_y \\ E_z \end{bmatrix} \quad (3.1)$$

Being P the polarization, ϵ_0 the electric permittivity at the void, χ the electric susceptibility and E the electric field, expressed in cartesian coordinates (x , y , and z).

The physical interpretation to this matrix is that the electric force of the ions bounds apply a restoring force after the ion was moved previously (i.e., incident light), This restoring force might not be equal in all directions.

Assuming that the crystal does not absorb energy, the previous expression (3.1) can be diagonalized to:

$$\begin{bmatrix} P_x \\ P_y \\ P_z \end{bmatrix} = \epsilon_0 \begin{bmatrix} \chi_x & 0 & 0 \\ 0 & \chi_y & 0 \\ 0 & 0 & \chi_z \end{bmatrix} \begin{bmatrix} E_x \\ E_y \\ E_z \end{bmatrix} \quad (3.2)$$

Or equivalently without matrix notation:

$$P = x\epsilon_0\chi_x E_x + y\epsilon_0\chi_y E_y + z\epsilon_0\chi_z E_z \quad (3.2)$$

Inserting (3.2) into the wave equation, the following relation can be found²⁰:

$$\frac{k_x^2}{\frac{k^2 c^2}{\omega^2} - (1 + \chi_x)} + \frac{k_y^2}{\frac{k^2 c^2}{\omega^2} - (1 + \chi_y)} + \frac{k_z^2}{\frac{k^2 c^2}{\omega^2} - (1 + \chi_z)} = \frac{\omega^2}{c^2} \quad (3.3)$$

Where k -vector has been related to the susceptibility parameters of the material. ω refer to the angular frequency and c to the speed of light at vacuum.

Defining the refractive index as:

$$n = \frac{kc}{\omega} \quad (3.4)$$

As well as:

$$n_x \equiv \sqrt{1 + \chi_x} \quad (3.4.1)$$

$$n_y \equiv \sqrt{1 + \chi_y} \quad (3.4.2)$$

$$n_z \equiv \sqrt{1 + \chi_z} \quad (3.4.3)$$

And substituting (3.4), (3.4.1), (3.4.2), and (3.4.3) in the dispersion relation (3.3); after simplifying the k -vector into an unitary vector and a scalar component ($\bar{\mathbf{k}} = k\hat{\mathbf{u}}$), it is obtained:

$$\frac{u_x^2}{(n^2 - n_x^2)} + \frac{u_y^2}{\frac{k^2 c^2}{\omega^2} - (1 + \chi_y)} + \frac{u_z^2}{\frac{k^2 c^2}{\omega^2} - (1 + \chi_z)} = \frac{\omega^2}{c^2} \quad (3.5)$$

This allows to relate the refractive index with the direction of the k -vector. Solving this equation will give rise to a double solution. Focusing on the case of a uniaxial crystal, in this case, two of the three susceptibility coefficients χ_x , χ_y and χ_z will be the same. This creates only an optic axis for the crystal, the z -axis by convention ($\chi_x = \chi_y \neq \chi_z$). The unique index of refraction is called the **extraordinary index** ($n_z = n_e$), and the other index is called the **ordinary index** ($n_x = n_y \neq n_z$).

To calculate the angle-dependent refractive index $n_e(\theta)$ or n_{eff} ²¹

$$n = n_e(\theta) = \frac{n_o n_e}{\sqrt{n_o^2 \sin^2(\theta) + n_e^2 \cos^2(\theta)}} \quad (3.6)$$

Being θ the polar angle measured from the z -axis of the crystal.

Figure 7 shows the angle dependance stated at the expression above. Depending on the direction of incidence, it can be seen a different extraordinary index. This type of representation is quite common when representing the optical axis of a material. By cutting a cross-section, as it has been done at Figure 7 (a), (b) and (c); it can be quickly seen the refractive indexes seen by the incident wave.

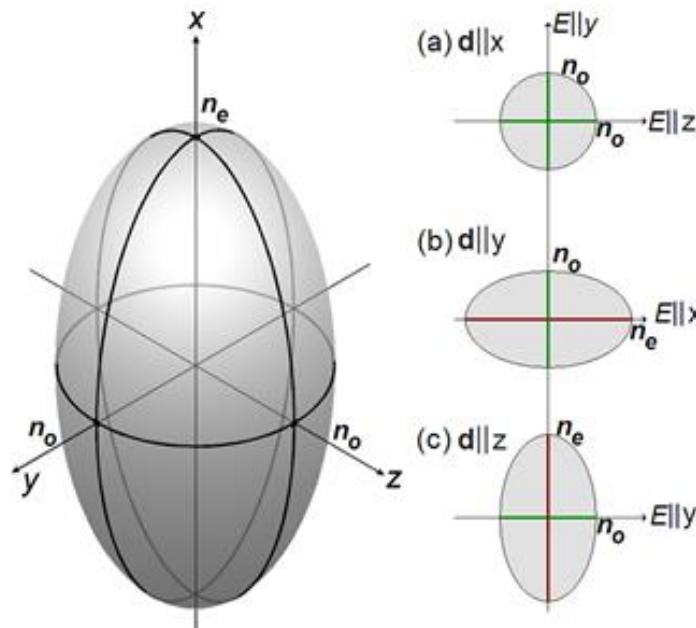


Figure 7: Refractive index ellipsoid. Special cases for direction of propagation parallel to (a) x axis, (b) y axis and (c) z axis.²²

3.2. Liquid Crystals

The key material for the development of this Master Thesis will be liquid crystals. They present peculiar properties quite useful for optical purposes. In this case, the focus will lay on how it is structured internally. Liquid crystals are mesophases between crystalline solids and liquids.

The molecules in this kind of material are highly anisotropic in shape. This is, they can be elongated, disc-shaped, lath-like, or more complex shapes. This, together with the fact that its molecules can be arranged applying an electric field, will generate an effect of birefringence from which will be taken advantage to steer a light beam source.

At a first classification for LCs, they can be divided into thermotropic, lyotropic and metallotropic depending on which physical property modifies their inner structure.

Among the possible phases from thermotropic LCs, the one of interest for this work is the **nematic phase** (Figure 8). In this state, the rod-like molecules have no positional order, although they self-align with their long axes roughly parallel. Most nematics are uniaxial, so that they have a longer axis, with the other two being equivalent. Most of these LCs contain benzene rings, so that their electrons can easily be moved by an electric field. This gives rise to dipoles able to rotate, making this an ideal medium to build devices based on nonlinear optical effects and light manipulation.

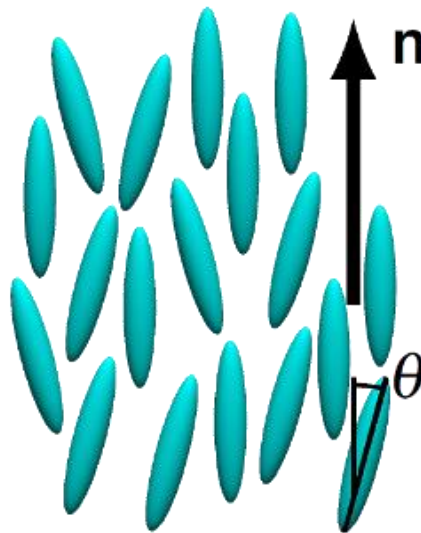


Figure 8: Nematic phase²³.

3.3. Liquid crystal optically phased arrays

Due to the wave nature of light, two waves with a difference in phase of $2k\pi$ for $k \in \mathbb{Z}$ are completely the same given that there was no change in amplitude. This is the reasoning behind a Fresnel lens (Figure 9). In this case, the lens material where the phase exceeds 2π is erased, giving rise to much more compact lenses that are able to focus on the same point.

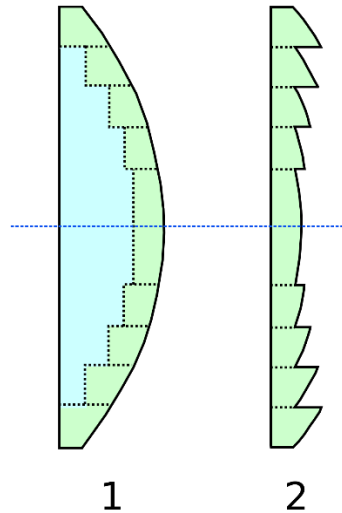


Figure 9: Equivalent Fresnel lens²⁴.

It will be taken in this case an analogous approximation. Steering can be accomplished using a wedge prism under the same principle. Being the index of refraction of the prism larger than the air, the light will travel slower when crossing it. The light through the thick part will be delayed in comparison to the one that goes through the thin part. A delay will be generated among the individual wave sources that will sum coherently in a different direction than the input one, giving as a result the change of the propagation direction.

Analogously, changing the refractive index, a delay could be induced at specific parts of the wave. If it could be changed the refractive index of a prism, light will be steered at different angles.

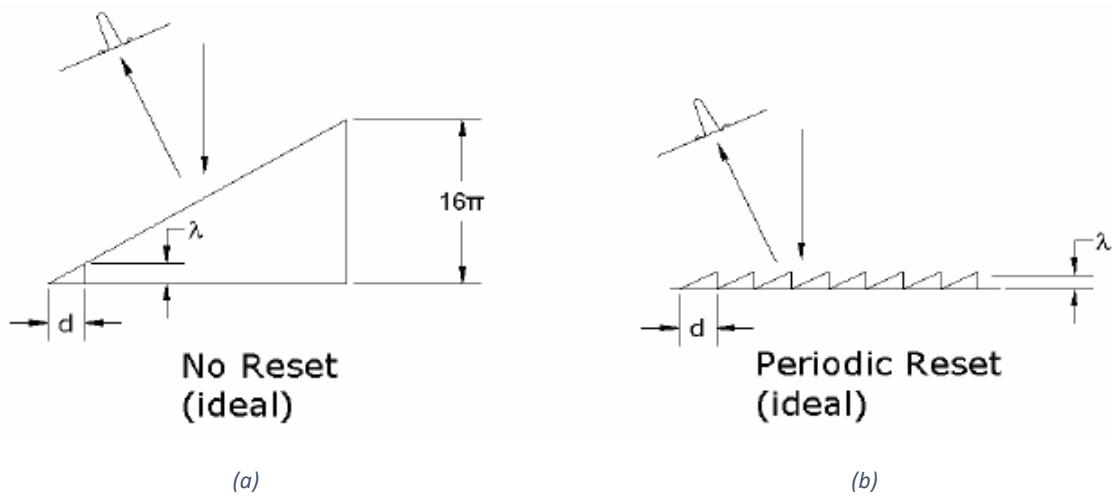


Figure 10: Concept of a LC OPA. (a) Phase distribution without reset and (b) with reset at λ or 2π .²⁵

That is the behavior that will be emulated in the LC-OPA (Figure 10). Zones where the light will see different delays will be generated polarizing the LC molecules. Two main schemes will be presented, shown in Figure 11.

Figure 11 (a) shows one known as **variable period grating** (VPG). In this case, the steering angle θ_s is given by $\sin\theta_s = \Delta\phi_s/k_0d$, where $\Delta\phi_s$ is the phase step between two adjacent electrodes, k_0 the vacuum wavenumber and d the width of electrode and gap.

Figure 11 (b) shows the scheme of **blazing grating** (VBG). In this case, periodic spots, or grating lobes, will be generated on the far field. The profile of the grating lobes is given by the modulation function of one period, and the angular position of the m th order grating lobe θ_m is determined by $\sin\theta_s = m\lambda_0/T$, where T is the modulation period. Similarly, to find the first order lobe in a discrete device, the relation will be $\sin\theta_s = \lambda_0/Nd$, where λ_0 is the vacuum wavelength and N the number of electrodes in one period.²⁶ This will be the scheme used at the device of this work.

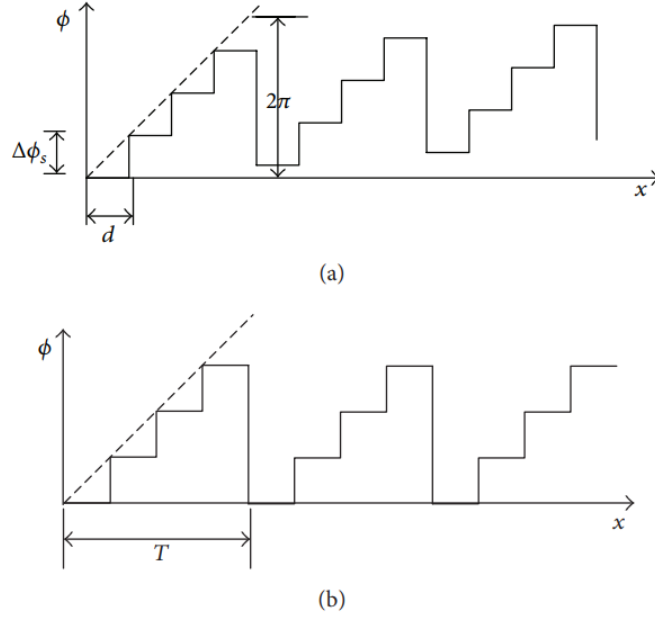


Figure 11: Phase modulation of LC-OPA. (a) VPG and (b) VBG ²⁶.

3.4. Device summary

Derived from the information presented above, some relationships that will be extremely useful in order to develop and characterize the device could be pointed out into a separate section.

Assuming that the incoming light is polarized, due to the uniaxial birefringence of the nematic LC employed, the delay δ could be calculated measuring the interference between the light polarized along the ordinary and extraordinary axes using crossed polarizers as a function of the applied voltage²⁷

$$\delta(V) = \frac{2\pi}{\lambda} \cdot [n_{eff}(V) - n_o] \cdot d \quad (3.7)$$

Where $n_{eff}(V)$ and n_o are the extraordinary effective and ordinary refractive indexes of the LC, d the thickness of the cell, and λ the wavelength of the input light.

The intensity variation follows a quadratic expression depending on the delay seen by the light:

$$I \propto \sin^2 \frac{\delta(V)}{2} \quad (3.8)$$

As a way to measure the amount of induced phase at the extraordinary axis in the device, a new concept will be introduced for convenience. The phase scheme used wrap the values between 0 and 2π . The term **topology** will be used to describe the number of times that the phase reset,

or go from 0 to 2π , along all the electrodes of the device. In other words, it will describe the total retardation of an equivalent prism in which the maximum value or the phase will be $t \cdot 2\pi$, being t the topology number.

In case that the topology is not an integer, multiple of the number of electrodes, the phase will be assigned interpolating the values to get the adequate levels. Figure 12 shows this procedure, emphasizing in bright colors the wrapped phase delay of each electrode.

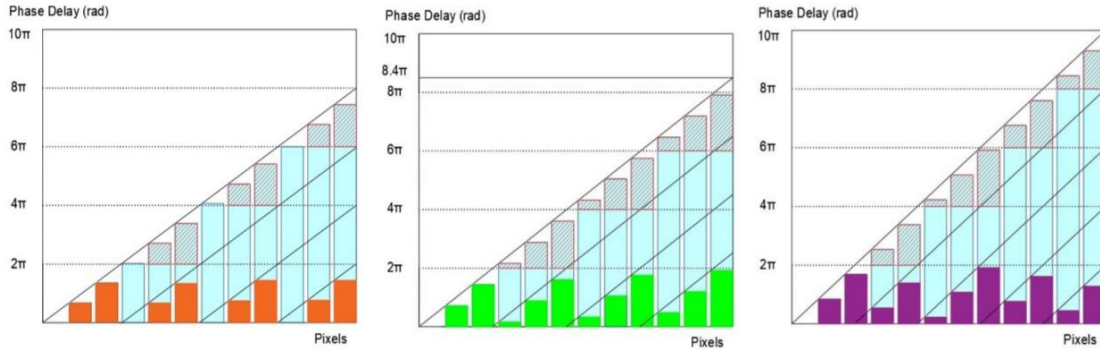


Figure 12: VBG scheme with 12 pixels. Topologies +4(left), +4.2(center) and +5(right) ²⁹.

4. Device design

This chapter will explain the different parts of the device and how they were designed. The layer structure will be presented, as well as the CAD drawing for the pixelated ITO layer.

4.1. LC cells

The project that will be presented is based on phase diffraction gratings, which were already introduced at the theoretical background section. Having a blaze grating scheme, a saw-tooth refractive index profile will be seen, due to the discretized approximation. Analog or continuous shapes could be achieved using high resistivity electrodes²⁸. The phase will be set individually for each pixel.

The approach followed in the design will be presented in Figure 13. Two glass wafers coated with Indium-Tin Oxide (ITO), a transparent and conductive material, will be used to make a sandwich filled with nematic liquid crystal. One of them will be used to inscribe the pixels using a Direct Laser Writing technique (**back-scribing**). A UV laser will be used with CNC controlled stage that moves the substrate in XY while maintaining the focal distance using a second laser feedback system. The other one will work as the ground plane.

It is important to note that over both ITO layers will be deposited a layer of polyimide, which will be latter rubbed. This is made to ensure a uniform, homogeneous and known LC alignment.

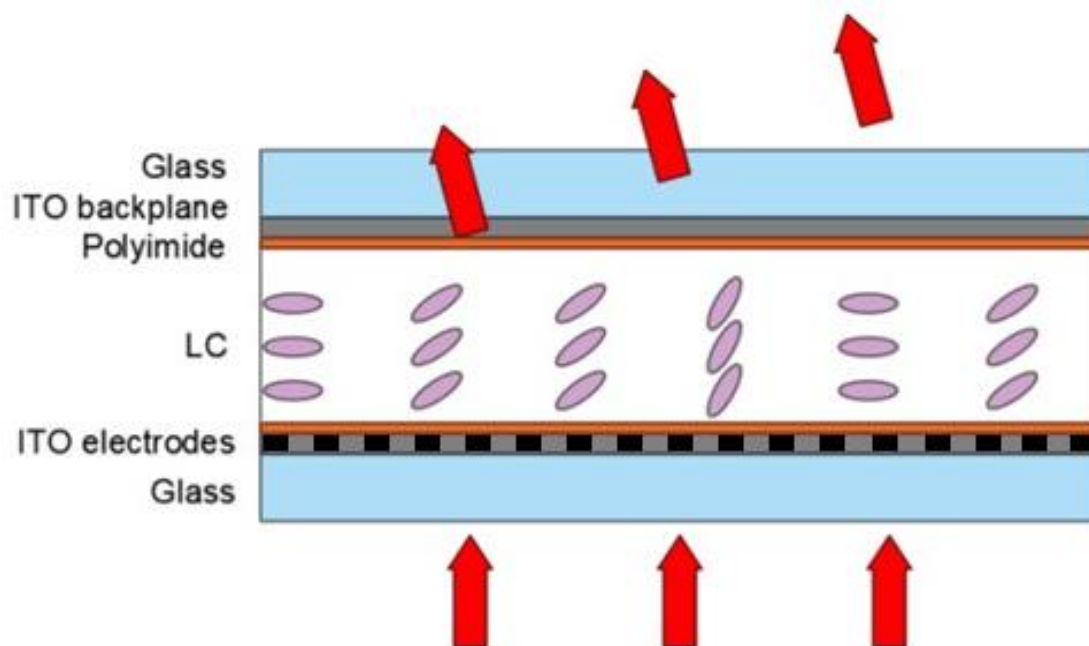


Figure 13: Diagram of a LC-OPA cell²⁹.

The final device will be constituted by two cells, each one in charge of steering the angle in one dimension. They will be controlled electronically separately so that each dimension could be altered without interfering the other one.

To create the digital design for the pixelated layer, a CAD application will be used (Figure 14). Due to the PCBs limits, a design with 144 electrodes was proposed. Each one of the up and down faces will count with 72 identical electrodes that will be controlled by one PCB. Both PCBs will be coordinated by the same LabVIEW routine.

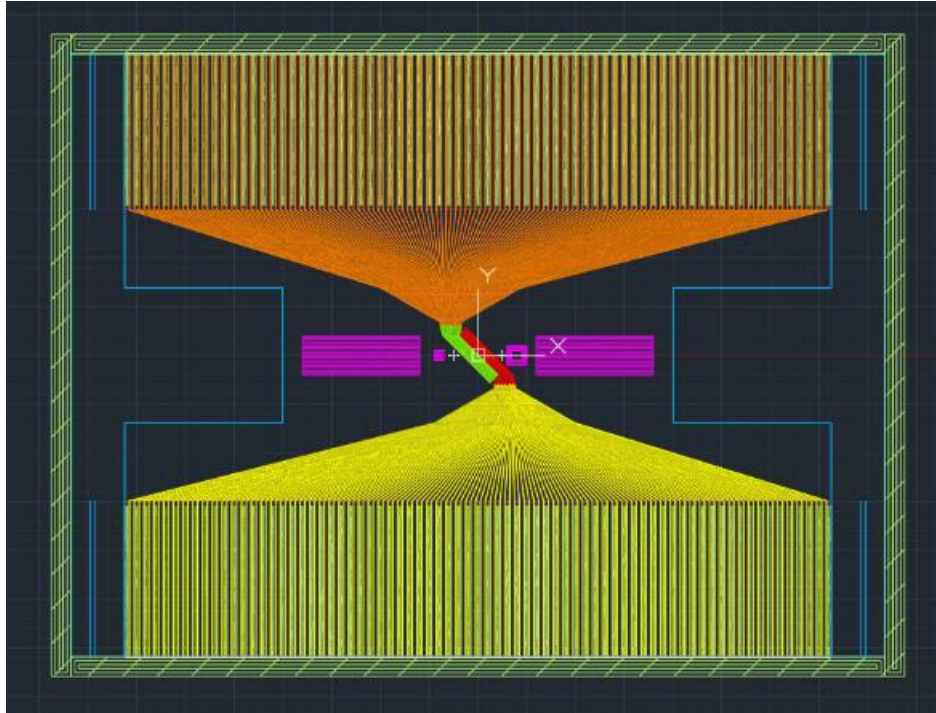


Figure 14: CAD complete design. Includes (red and green) active zone, (orange and yellow) fanout, (purple and white) alignment marks, and (blue and light yellow) ground.

The pitch for the active area elected is $7,5 \mu\text{m}$. This will result in a total width (with the 144 electrodes) of $1080 \mu\text{m}$. The electrodes will grow until reaching a width of $250 \mu\text{m}$, equally spaced between them by $250 \mu\text{m}$.

The active zone will have an inclination of 45° with respect the X and Y plane as could be seen at Figure 14 and Figure 15 (a). Flipping the cell with respect Y plane, obtaining an inclination of -45° , will steer the angle in the orthogonal dimension. This way, the same design can be used to steer the beam in both dimensions and maintain the connection points in two (upper and lower sides).

During the design of the CAD drawing, tolerances of the manufacturing process had to be taken into account. Due to the laser beam width and its focusing systems, the pitch of the active zone had to be limited. Lower widths could give rise to erasing too much ITO, ending up having a low fill ratio or in the worst case, cutting the electrodes. This last one is also the reasoning behind the triangular shape at the fanout section (yellow-down and orange-up at Figure 14), built to allow better angles and distances between electrodes while they grow till reaching the size of the PCB ones.

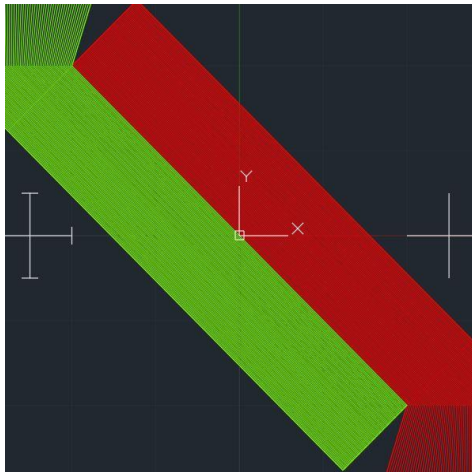
It had to be included hatch sections at the interpixel zones (non-conductive space between electrodes) in order to avoid short circuit between two continuous pixels.

In order to outline specific points of the design, some zoomed images were taken to detail Figure 15:

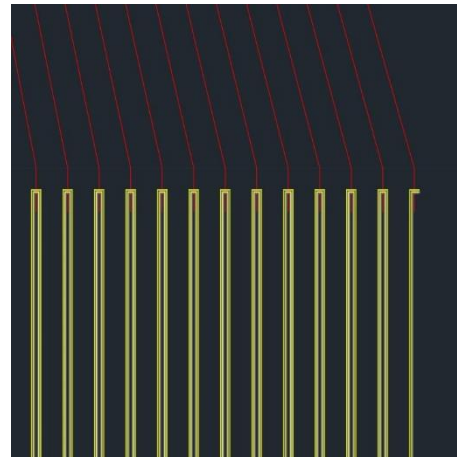
- Figure 15 (a) shows the detail of the active zone. As it was mentioned before, two halves of 72 electrodes each can be clearly seen.
- At Figure 15 (b), it is shown the connection between the fanout and the active zone. Interpixels are cut multiple times, with some margin to avoid thermal expansion issues,

to ensure connectivity between fanout and the active area (each defined in separate layers in the CAD and written by the laser in succession).

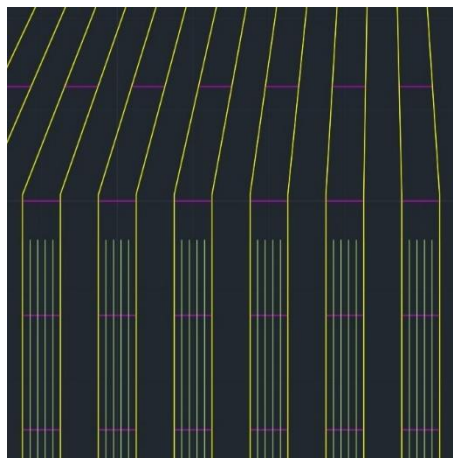
- In Figure 15 (c), it can be seen the structure of the scratches or hatches at the interpixel. Its extension is limited to the fanout zone.
- Figure 15 (d) shows two identical cells to the one in Figure 14 overlapped. By only flipping the same design, all the main elements stay perfectly aligned, even the connection points.
- In Figure 15 (e) a zoom of the overlapped cells is presented, where it is shown the square region of interest which will constitute the device work zone to steer the beam.



(a)



(b)



(c)

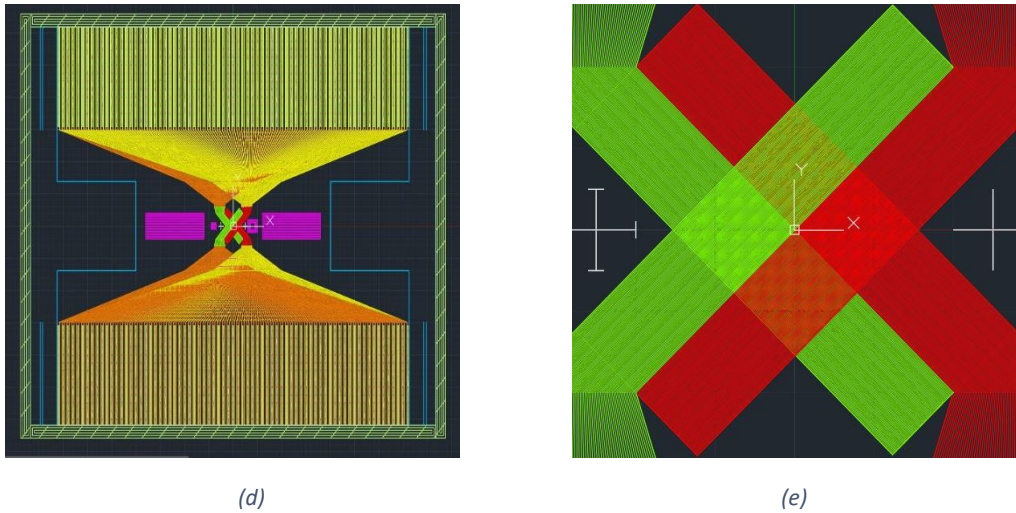


Figure 15: Details from CAD design. (a) Zoom of active zone. (b) Connection between active zone and fanout. (c) Interpixel hatch. (d) Overlapped cells. (e) Zoom of overlapped active zone.

4.2. Electronic driver

To control the driven voltage of the cell electrodes, specific PCB designs from CEMDATIC (Figure 16) will be used. Three PWM LED drivers, specifically the model TLC5947 from Texas Instruments, with 24 outputs will control the device. The output will be adjusted by using a control resistance of 18 k Ω and a 10 k Ω pull-up resistor; and then inserted into the digital input of an analogue switch (ADG5413, Analog Devices), which will select between a signal from a function generator (in this case, a squared profile, 10 V_{pp}, 1 kHz signal) and ground²⁹.

Each of the boards will be able to control 72 electrodes. Combining two by daisy chaining them, the capability could be extended to 144 electrodes. For the LC devices that are discussed in this work, four boards will be used connected in pairs to drive the desired voltage. The cycle of this signal will be set from a LabVIEW routine (see Annex 10.3) that will communicate with an Arduino module via SPI.

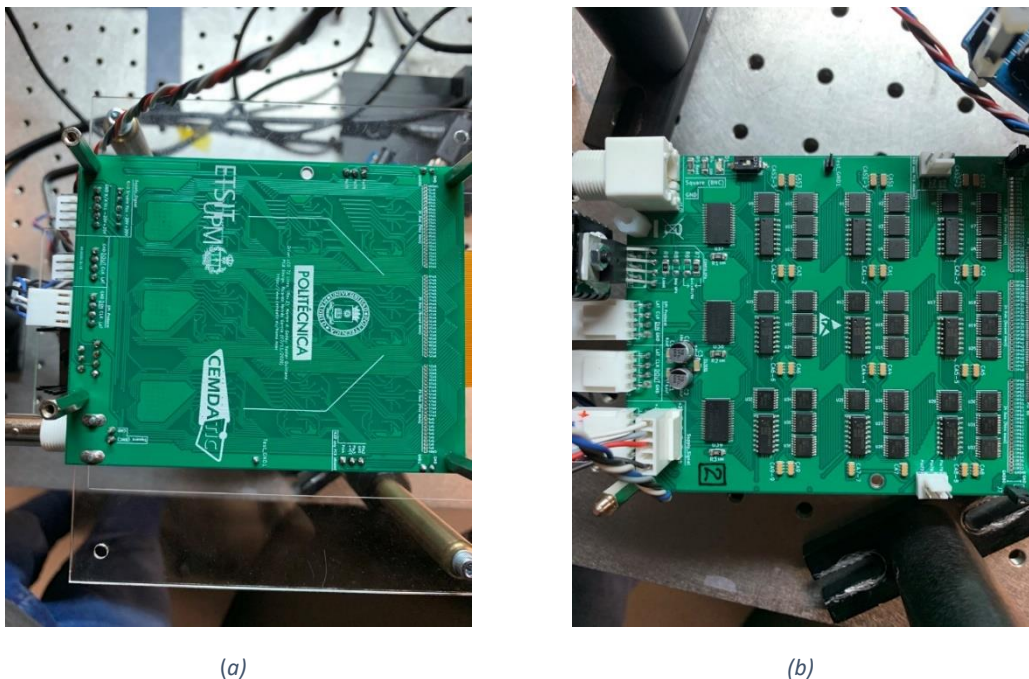


Figure 16: Electronic driver. (a) Back side of the board. (b) Front side of the board.

5. Manufacturing

The manufacturing process will take place at the ETSIT facilities, from the Technical University of Madrid. Specifically at the Clean Room of the investigation group CEMDATIC. The methodology will be described to manufacture the device, paying special attention to the materials and instrumentation employed.

5.1. Steps to manufacture the LC-OPA cell

5.1.1. Wafer cutting

The first step will be cutting the glass wafers at the proper dimensions (Figure 17). The size chosen for the pixelated crystal will be 35x50 mm, and 20x50 for the backplane. Prior to this, a layer of polyvinylpyrrolidone (PVP) will be spread over the ITO face in order to protect the wafer from undesired scratches from glass shards. Once finished this process, the PVP must be removed.

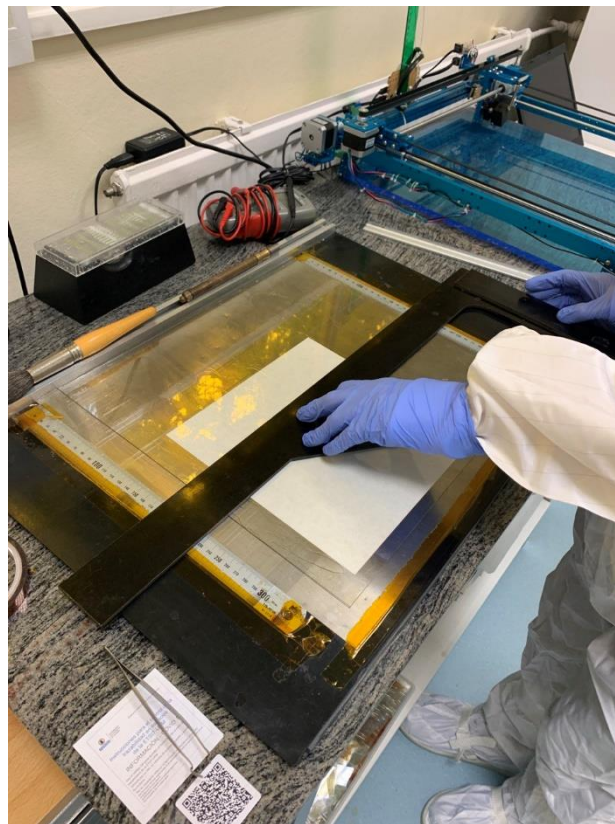


Figure 17: Wafer cutting process.

5.1.2. Laser scribing

CEMDATIC owns a pulsed laser (Figure 18), with a tunable frequency between 20 and 300 kHz, an average power of 300 mW and a wavelength of 355 nm. The laser has a 3 axis CNC stage controlled by computer with a movement precision under one micron.



Figure 18: CEMDATIC clean room laser.

Three optical schemes could be differentiated at it (Figure 19). The first one (in yellow) is in charge of generating a visible image of the process. The light from a LED will reach a power splitter, sending light to the sample. Light will be also reflected in the opposite way, reaching a camera that will collect the image. The second one (in red) will maintain the focus of the laser on the sample through another laser and a feedback loop. The third one will be used for laser ablation or direct writing techniques. It will be composed by the laser, a chain of mirrors, lenses, and a variable attenuator.

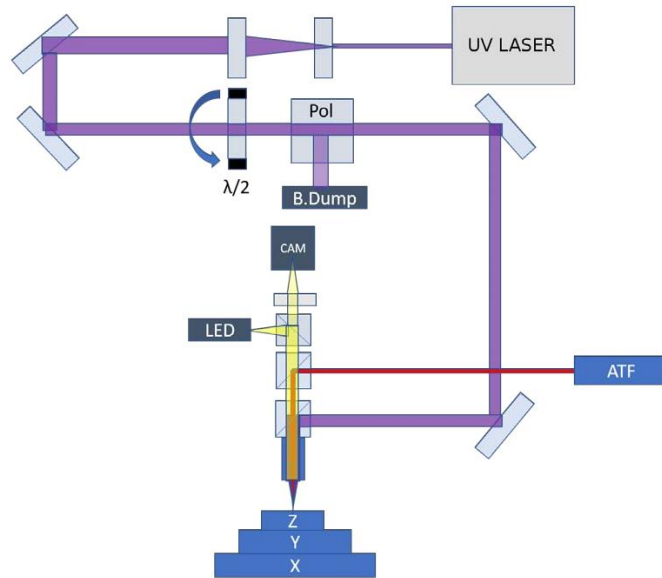
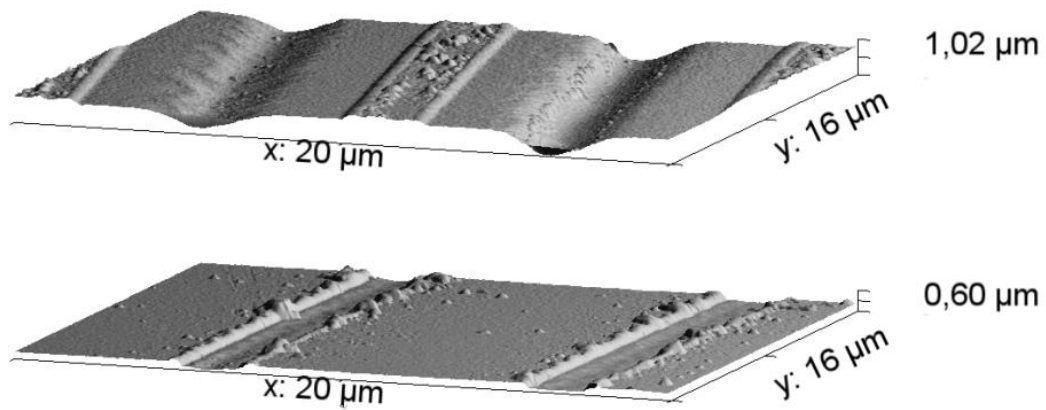
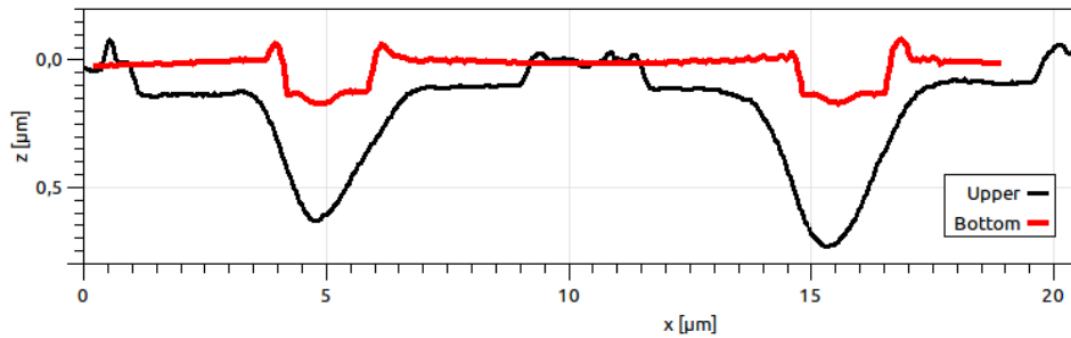


Figure 19: Clean room laser - optical setup³⁰.

For this manufacturing process, the ITO layer is attacked from the back surface. The main advantage of back scribing in comparison with making the laser incises directly on the upper face is the finesse that could be achieved with the first one. With upper ablation, to erase specific lines of ITO for creating the electrodes and assure that the tracks will not be interconnected, it is necessary to apply too much power. This will lead to a bigger width of the lines which is, for the device, a completely undesirable effect. Bottom ablation does not need the same levels of energy and obtains an erasing profile sharper and smaller, as could be seen in Figure 20³⁰.



(a)



(b)

Figure 20: AFM image (a) and measured profile (b) for upper and bottom ablation. The power employed at the back-scribing is three times lower than the front-scribing³⁰.

The CAD design will be exported into two CNC files: one for the active zone and another for the remaining design. This will allow setting different configurations at the laser for each of them. The one of the active zone will employ the 15% of the available power, whereas the fanout will use the 50%. The frequency used in both cases will be 50 kHz, with an intensity of 5,2 A.

5.1.3. Silver contact and rubbing direction

To create an interconnexion between the ground sections of the glass wafers that compound the cell, conductive silverpaste will be used.

Kapton tape prevents that any polyimide reaches the contact area and marks will not be erased. Markers in the ITO layer the specifies where the silverpaste must be situated, and the wanted rubbing direction for that glass wafer.

5.1.4. UV treatment

In order to facilitate the following step, the glass wafers will be treated with UV radiation. The aim of this process is to remove contaminant molecules of photoresists, resins, human skin oils, cleaning solvent residues or silicone oils from the wafers to have its surfaces as clean as possible³¹. In addition to this, the layers will gain hydrophilic properties, making easier coating the following layers.



Figure 21: Jetlight UVO-Cleaner® model 18.

In this case, the wafers will be treated for around 10 minutes with the UVO-Cleaner® (Figure 21).

5.1.5. Alignment layer

After this, a layer of polyimide PIA 2304 (Chisso LIXON aligner, Tokyo, Japan), will be deposited over the ITO. The polyimide is an organic compound employed to pre-determine the molecule alignment in LC devices.

After properly cleaning the glass wafers, a fine layer of this material will be spin-coated over the ITO with the help of a spinner (Figure 22). For this step, the rpm will be set to 2500. Polyimide will be poured at the center of the wafer and will be spun for 30 s.

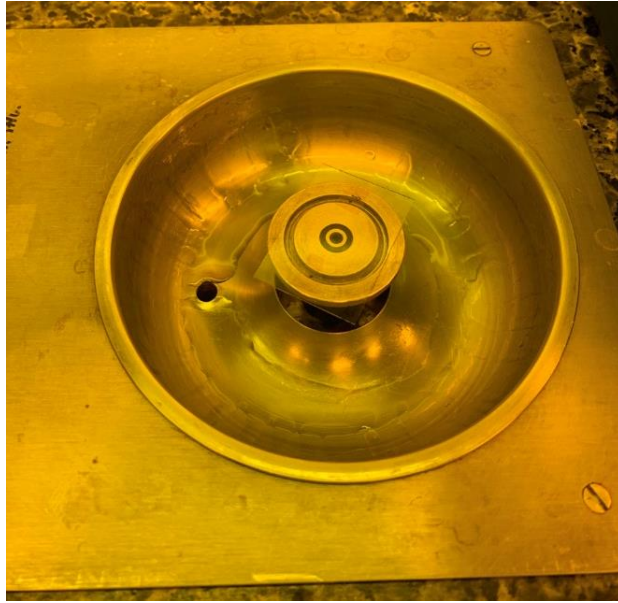


Figure 22: Lab rotatory disk.

During this process, an auxiliary hotplate will be used (Figure 23), set to 150 °C to start the process of curing the material and evaporate the solvent of the polyimide mixture.



Figure 23: Lab hotplate.

Once all the wafers have been treated with polyimide, the samples will be put into an oven at 180 °C for around 45 minutes to completely cure the deposited layer.

Once cured, the material will be rubbed with a roller (Figure 24). This will charge electrically the polyimide and will align homogeneously the nematic LC.³² The substrates with the counter electrode will also follow this process.

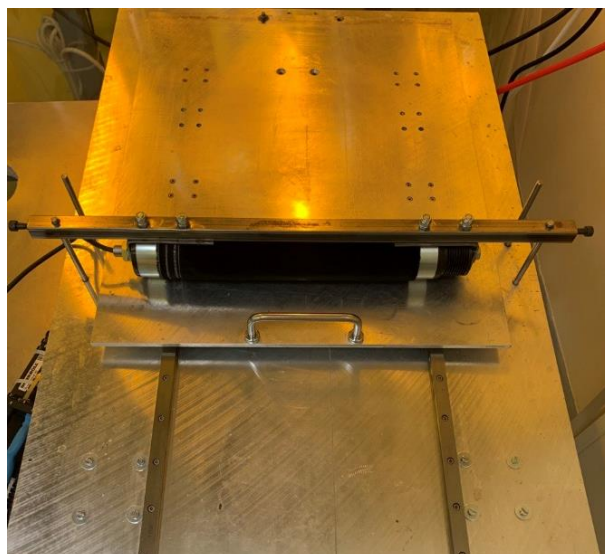


Figure 24: Lab roller.

The orientation of the rubbing will be reverse in the case of the non-scribed wafers. The objective is obtaining a homogeneous alignment along all the LC. If the alignment is done in parallel, the inner structure will have a gradient in the inclination of the molecules between both layers³³. At Figure 25, the molecule orientation can be seen with an orthogonal alignment (left) and parallel (right).

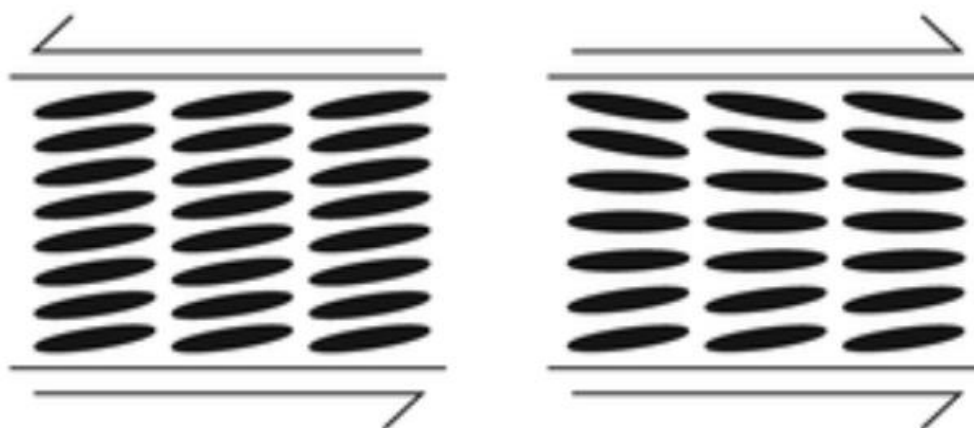


Figure 25: Effect of rubbing at LC orientation³³.

5.1.6. Spacers layer

In order to control the thickness of the cell a layer of 'spacers' will be included, discrete elements that will create a regulated space between both wafers. In this case, the material employed will count with cylindrical silica particles of 7.2 μm .

The spacers will be diluted in acetone. To avoid the creation of clusters in this dilution, an ultrasonic bath device from JP Selecta, model Ultrasons (Figure 26) will be employed. This equipment will make the liquid vibrate with ultrasounds so that these clusters disappear.



Figure 26: Ultrasounds bath machine.

Spacer will be deposited used the spinner at 1500 rpm during approximately 30 s to uniformly distribute the spacers over the substrate.

Special care must be taken in this case, as the mix is very volatile. Evaporation of the solvent may lead to non-uniform spacer distribution affecting the transmittance of the cell.

5.1.7. Cell assembly

Once all the layers have been prepared, two wafers of each kind (pixelated and non-pixelated) will be used to mount the cell. First, the silverpaste will be taken to create the interconnexion between planes. With the help of a thin wire, the silverpaste will be deposited the zones that have been marked therefore.

After this, three of the cell sides will be sealed with a two component epoxy adhesive. The cell will be left drying for a complete day. To ensure cell thickness homogeneity pliers will be employed until it is completely dry (Figure 27).



Figure 27: Cell gluing.

5.1.8. LC filling

At this step, a vacuum bell will be used. The material employed as LC will be MDA 98-1602 ($n_e=1.78$ and $n_o=1.52$, Merck KGaA)³⁴.

A small amount of LC is poured into a metallic base and placed inside the vacuum bell. At the same time, the cell will be situated into a piece whose movement could be controlled by the operator. For about one hour, the air from the cell and the LC will be extracted actioning the vacuum pump. After this, the cell will be shifted down until the unglued side (that must be facing the LC container) is in contact with the LC. This position, shown in Figure 28, will be maintained for 30 minutes.



Figure 28: Vacuum bell.

Once the cell is filled, epoxy adhesive will be used again to seal the remaining side, enclosing completely the LC.

5.1.9. Electrodes implementation

Using an anisotropic conductive adhesive (ACA) (Hitachi Chemical, Tokyo, Japan), the flex of electrodes that will be the interface between the driver and the LC-OPA will be attached.

For this point, a programmable thermal press (Figure 29) will be used. It counts with two separate stages, with temperature and time of actioned press independently configurable. It also is equipped with a vacuum pump to avoid movements at the devices during the different processes and a couple of microscope cameras that allow to see in detail the zone where the press will be actioned, with regulators for the amount of light desired at it.



Figure 29: Thermal press.

The Hitachi adhesive counts with two sections. After cutting a piece of adhesive strip with the desired measures, the brown protective film will be removed and the ACA will be placed onto the cell, making sure that the adhesive reaches the electrodes. The first program of the press will be executed, ensuring that the adhesive strip is attached to the cell.

At this point, some Kapton will be put under the adhesive. This is done in order to avoid contacts from the electrode flex with the lower parts of the cell. In case that the outer designs that enclose the active zone and the fanout are not properly cut, these contacts could polarize the inner sections in an uncontrolled way.

Once assured this, the film from the white face will be removed and with the help of the cameras, the electrodes of the connecting flexible cable will be aligned with the ones from the substrate. The press is actioned again, sticking the flex to electrodes to the cell.

5.1.10. Output. Single cell

The resulting cell is presented in Figure 30. It will be composed by two crystals of different lengths, but similar width that will encapsulate the LC; and two flexes of 80 electrodes each (72 useful) that will be used as interface between the electronic driver and the cell.

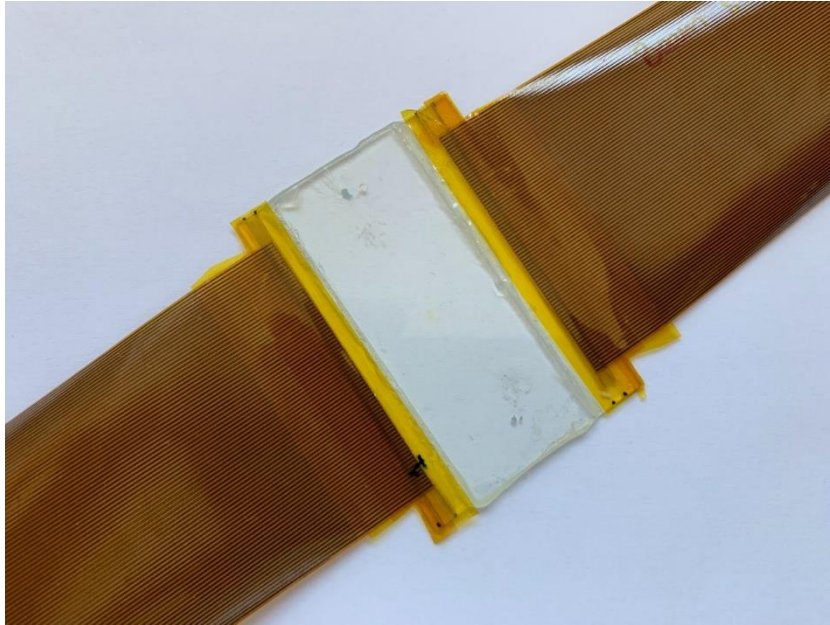


Figure 30: 1D device – “Sample 3”.

5.1.11. Cell alignment.

With the help of a microscope, the alignment marks introduced at the design of the pixelated layers will be used to overlap correctly the two cells that will compound the complete device.

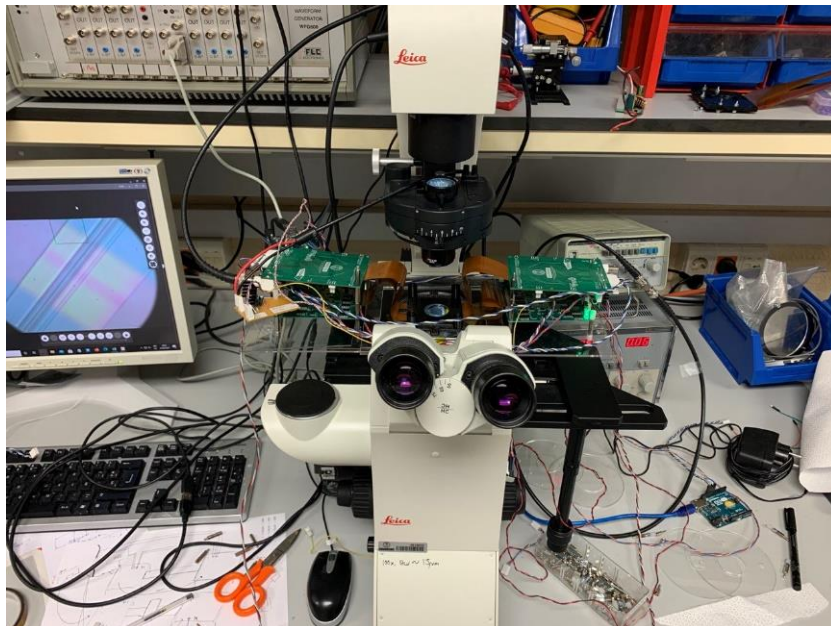


Figure 31: Cell alignment during 2D device assembly.

5.1.12. Output. 2D device.

The final device is shown at Figure 32. 288 electrodes, 144 per side, will control the complete device. The cells are fixed with the help of a polylactic acid (PLA) holder built in a 3D printer.

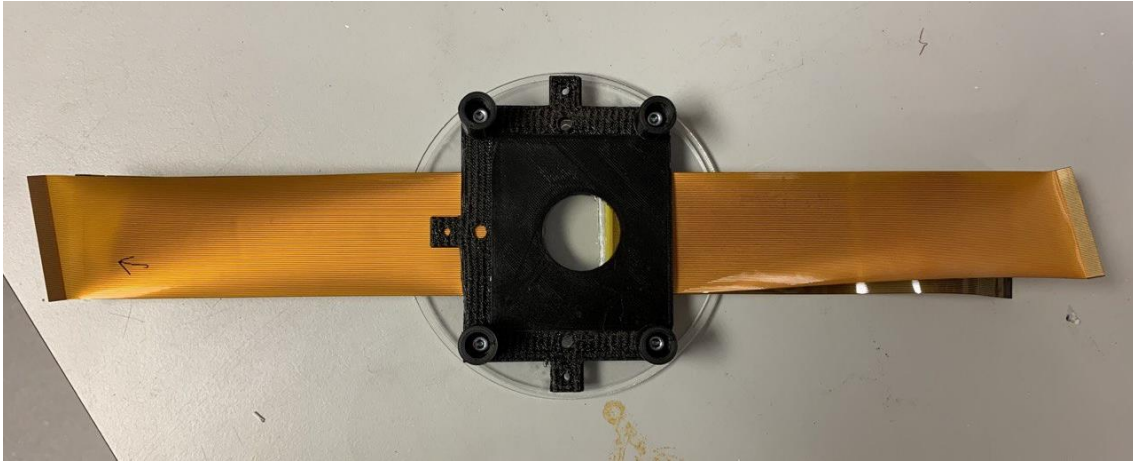
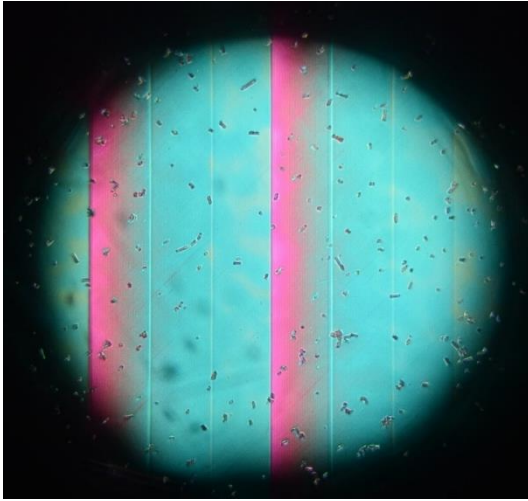


Figure 32: 2D device - "Sample 5" and "Sample 7".

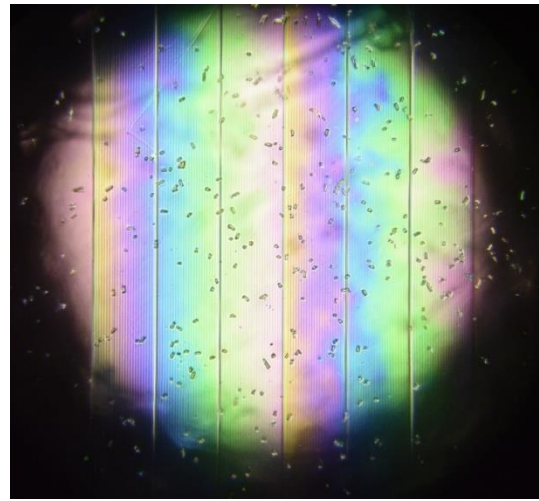
5.2. Common issues

Combining a manual manufacturing process with the design sizes, give rise to a lot of troubles. In this subsection, it will be tried to note the main ones related to the LC cells:

- 1. Glass wafers cleaning.** In case of not being working in a clean room, there will be plenty of particles that will be deposited on the devices. In addition to this, working with protective layers as the PVP could leave some residues that will affect the following steps success or the final device performance. In this case, it was needed to be continuously using acetone or filtered distilled water to keep them clean.
- 2. Laser output power.** Increasing the power of the laser will help to assure that the electrode tracks are well defined over the ITO, but in return, the width of the erased zone was increased. With this device, the manufacturing limit of the laser is reached, and it must be done a continuous trade-off. Both problems, not erasing ITO properly and short-circuit electrodes, and erasing too much ITO and suppressing electrodes, are perfectly plausible under the laser specifications.
- 3. Concentration of alignment and spacers layers.** Some of the cells manufactured presented wrong behaviors due to the deposition step. As an example, a polyimide with a dissolvent that made the density of the dilution quite high was employed at some of the cells. When used at the spinner, the thickness of the alignment layer varied quite among the different points, having an impact on the pre-tilt induced at the molecules and their behavior when a voltage is applied. The result could be seen at Figure 33 (b). Using a polarizer to be able to track the phase variation, non continuous zones could be easily identified in comparison to the more appropriate output of Figure 33 (a).



(a)



(b)

Figure 33: "Sample 1" (a) and "Sample 3" (b) microscope caption when using a Topology +2.

4. **Cell sealing.** It is extremely important to be careful during the cell assembly step. In this case, some troubles were faced due to the adhesive employed. Both at the void machine and out of it, air leaks were experimented making the device completely useless.

6. Characterization

6.1. Set-up

The cell will be characterized by establishing the relationship between the input PWM signal and the phase delay generated, to know the working points from the cells that will compose the final device.

The chain that will follow the light will be shown at Figure 34:

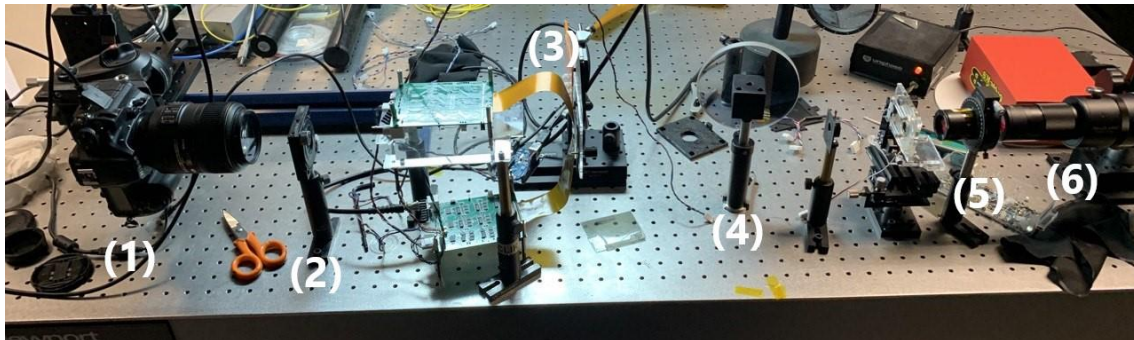


Figure 34: Characterization set-up.

From left to right, the light cross:

- (1) Camera.
- (2) -45° polarizer.
- (3) LC-OPA cell.
- (4) Attenuator.
- (5) 45° polarizer.
- (6) He-Ne laser of 632.8 nm.

In order to know that the polarizers are correctly aligned, a first set will be installed, composed only by the laser, both polarizers and the camera. The polarizers will be rotated until not seeing any light at the camera, so that its axes are completely perpendicular.

At the calibration set, the beam from the laser will be attenuated initially to not saturate the camera sensor. After this, it will cross the polarizer set to 45° . The device will be polarized vertically (in the image). This will generate a delay in the vertical component of the light, modifying the polarization of the wave. Positioning again a polarizer at -45° will allow seeing a change in the intensity that reaches the camera sensor, due to this phase rotation of the light components.

The characterization will be governed by a LabVIEW routine and the electronic driver. The LabVIEW routine will have different modules. The first one (Annex 10.3.2) will set the input voltage for each electrode. It will control the cycle of a PWM signal, whose 'ON' waveform will come from a function generator. For this setup, a square signal will be used with 10 V_{pp} and 1 kHz.

The second one (Annex 10.3.3) will control the camera remotely. It can modify parameters such as exposure time or focal distance and has a live view from the camera where it could be defined different regions of interest, where the light intensity will be measured. Picking different regions from the active zone of the device will help to determine if all the electrodes are polarizing the molecules in the same way.

The third module (Annex 10.3.1) will work as a sort of for loop that will take as sub modules the two previous ones. It charges an array, modifiable, expressed in bits with the different values of the PWM cycle that are wanted to be tested.

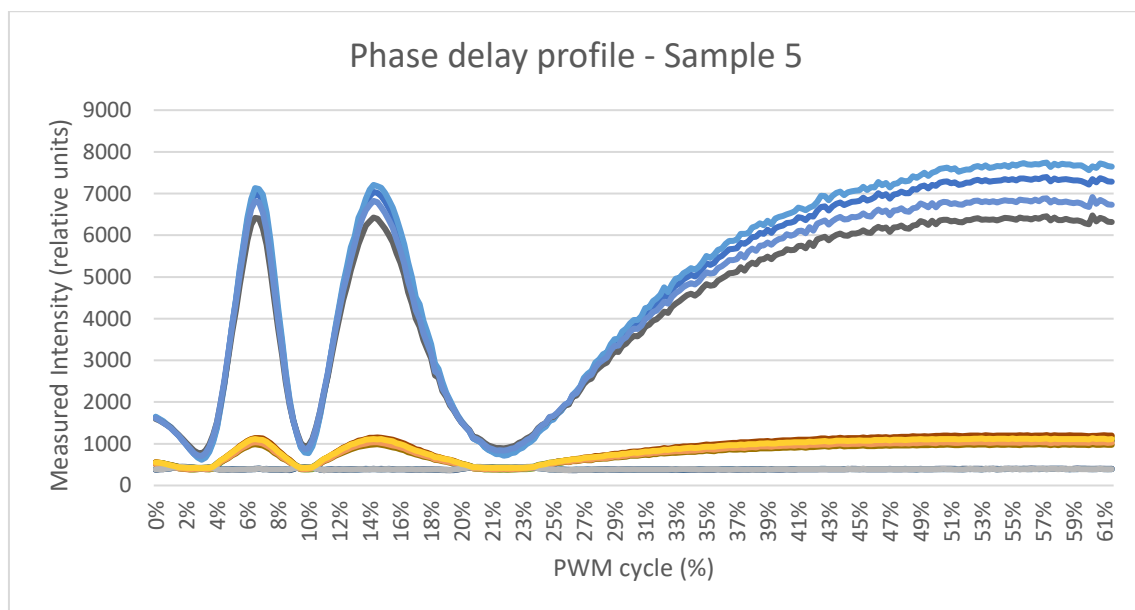
Once it has finished testing all the values, it exports the obtained values of light intensity expressed as a Bayer filter (two greens, one blue, one red) for each one of the regions of interest defined previously.

6.2. Results

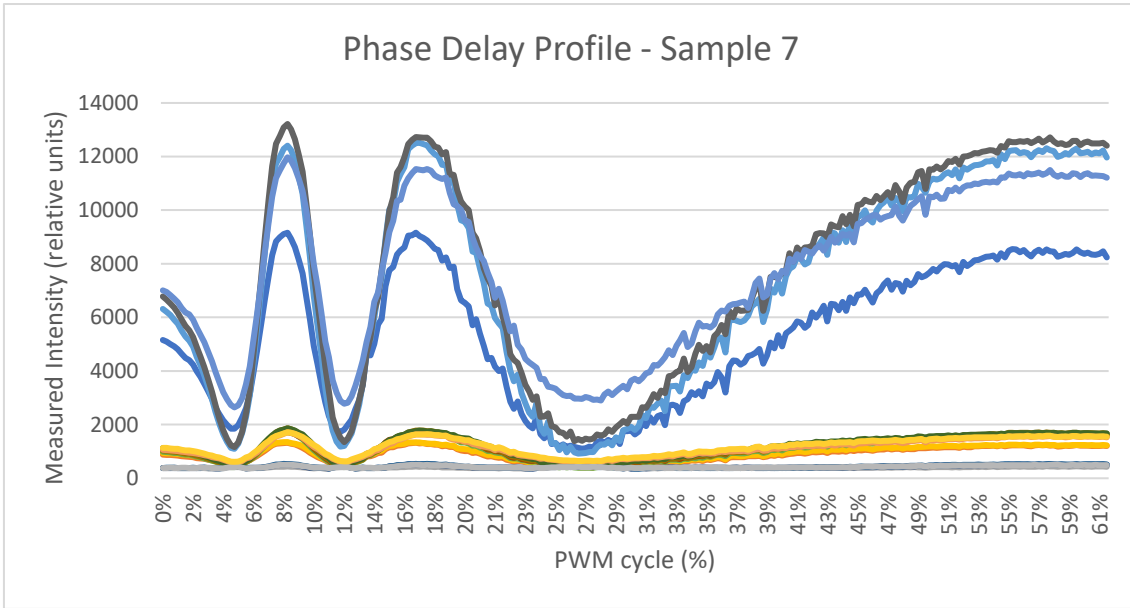
Differences are expected in this section for the different devices manufactured; since the light source is not uniform, and process of manufacturing is quite sensible. Small variations on it might modify slightly critical parameters such as the thickness of the cell.

10 operative cells were manufactured at the time this Thesis was written. In order not to fulfill this section with repetitive information, just the cells that will compound the final device will be presented. The internal names that receive these cells are "Sample 5" and "Sample 7" and this is how they will be presented at this work.

Given this, first it will be presented the intensity or phase variation as a function of the input voltage, at Figure 35 (a) and Figure 35 (b). The 4 RGBG components from the camera sensor will be taken for the plots. It can be quickly seen the profile for red components in comparison to the other ones, due to the use of a red laser. There will be 4 lines for each component due to the selection of 4 regions of interest from the LabVIEW routine.



(a)



(b)

Figure 35: Characterization charts. (a) "Sample 5", (b) "Sample 7".

The crystal molecules will reorient "switch" depending on the voltage, giving rise to a modification of the extraordinary refractive index. The phase delay will be shifted from 0 to 2π (and successive multiples), rotating the polarization and impeding part of the light cross the 2nd polarizer. As the cycle increases, the intensity reaches a saturation point. Too high cycles will impede the molecules get back to its rest or intermediate positions.

In order to generate a model to express analytically this relationship, a pseudo exponential decreasing function will be used.

$$\delta = A * e^{-B*dc} + C$$

A complete period from 0 to 2π will be taken to fit the curve. Using an optimization software (in this case, the Solver functionality from Excel), the parameters A, B and C will be obtained. The results obtained for the cells that will compose the final device are shown in Table 1.

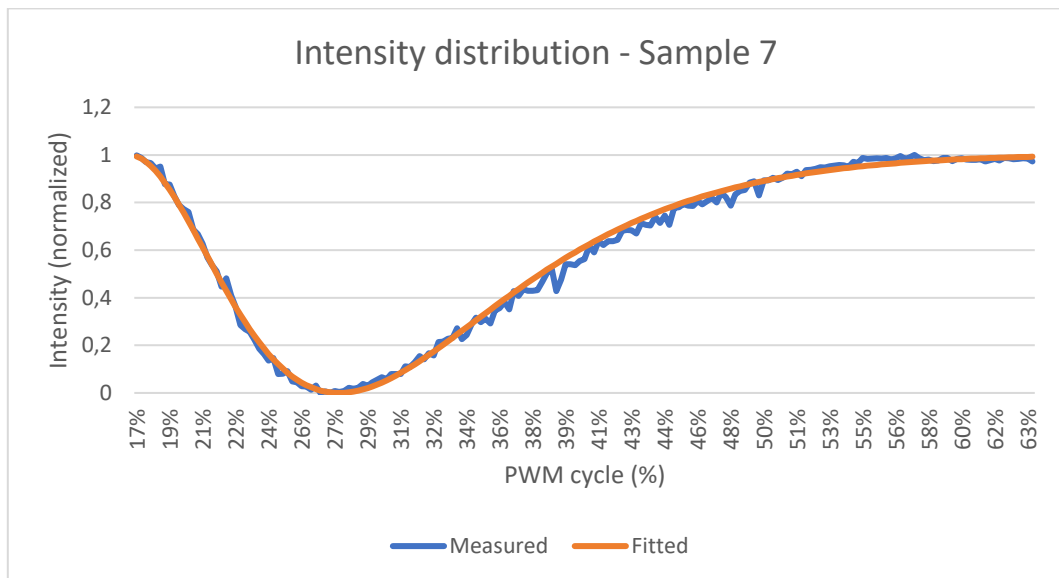
	Sample 5	Sample 7
A	19,2570	27,3866
B	-8,3049	-8,0265
C	3,2100	2,3192

Table 1: Model parameters for "Sample 5" and "Sample 7".

Figure 36 shows how the model adapts to the measured distribution. The interval picked to characterize the cells was the one comprised between 15-50% of the PWM cycle in both cases.



(a)



(b)

Figure 36: Measured intensity vs fitted intensity. (a) "Sample 5", (b) "Sample 7".

7. Simulation

7.1. Theoretical background

To build the simulation, some assumptions were made:

- 1) The contributions apart from the Active Zone are neglected.
- 2) The incident beam is perfectly gaussian, with a wavelength of 633 nm (He-Ne laser).
- 3) The measure screen is sufficiently far to consider being in 'far field'.

The main approach that will be followed is the Fraunhofer diffraction method, that allows having a scalar approximation for this experiment. Along this section, the formulas employed at the simulation will be derived, pointing out the reasons why the results might lose accuracy. For more details on how these steps were reached, please go to Chapters 1,2,3,4 from "Introduction to Fourier Optics" from Joseph W. Goodman³⁵, from where it was taken the majority of the information.

Skipping the approximations made at Kirchhoff and Sommerfeld diffraction formulas, this section will start from Huygens-Fresnel Principle of diffraction in order to lighten the mathematical deriving. Given this, the field at a random point P_0 is:

$$U(P_0) = \frac{1}{j\lambda} \iint_{\Sigma} U(P_1) \frac{\exp(jkr_{01})}{r_{01}} \cos\theta \, dS \quad (7.1)$$

Where n is the normal vector of the aperture, P_1 a random point of the aperture, θ the angle between n direction and P_1 a random point at the aperture. Being the cosine:

$$\cos\theta = \frac{z}{r_{01}} \quad (7.2)$$

Could be rewritten Huygens-Fresnel principle, in rectangular coordinates as:

$$U(x, y) = \frac{z}{j\lambda} \iint_{\Sigma} U(\xi, \eta) \frac{\exp(jkr_{01})}{r_{01}^2} \, d\xi d\eta \quad (7.3)$$

Where ξ and η represent the rectangular coordinates at the origin plane. To clarify this, at Figure 37 can be found a graphical representation.

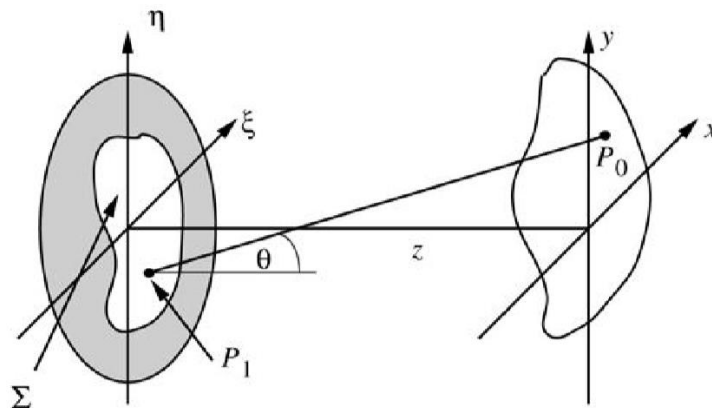


Figure 37: Diffraction geometry³⁵.

To reach this point, two approximations were made. First, taking a scalar approach, and second that the observation distance is many wavelengths away $r_{01} \gg \lambda$.

A binomial expansion will be used at the distance r_{01} to reach a simpler expression (Fresnel Approximation). Being b a number less than unity, the binomial expansion of the square root is

$$\sqrt{1+b} = 1 + \frac{1}{2}b - \frac{1}{8}b^2 + \dots \quad (7.4)$$

The first two terms of the approximation will be retained. Although r_{01} at the denominator will not suffer a high error, the one in the exponential can generate with small changes of the phase a great shift of the value.

$$r_{01} = z \sqrt{1 + \left(\frac{x-\xi}{z}\right)^2 + \left(\frac{y-\eta}{z}\right)^2} \quad (7.5)$$

$$r_{01} \approx z \left[1 + \frac{1}{2} \left(\frac{x-\xi}{z}\right)^2 + \frac{1}{2} \left(\frac{y-\eta}{z}\right)^2 \right]$$

Rewriting (7.3) substituting (7.5) into it:

$$U(x, y, z) = \frac{z}{j\lambda} \iint_{\Sigma} U(\xi, \eta, 0) \exp \left\{ j \frac{k}{2z} [(x-\xi)^2 + (y-\eta)^2] \right\} d\xi d\eta \quad (7.6)$$

And reorganizing the exponential:

$$U(x, y, z) = \frac{e^{jkz}}{j\lambda z} e^{j\frac{k}{2z}(x^2+y^2)} \iint_{-\infty}^{\infty} \left[U(\xi, \eta, 0) e^{j\frac{k}{2z}(\xi^2+\eta^2)} \right] e^{-j\frac{2\pi}{\lambda z}(x\xi+y\eta)} d\xi d\eta \quad (7.7)$$

Which turned out to be the Fourier transform of the product of the aperture distribution $U(\xi, \eta)$ just at the right of the aperture and a quadratic-phase exponential $\exp(j(k/2z)(\xi^2 + \eta^2))$.

Making another assumption (*Fraunhofer far field* approximation):

$$z \gg \frac{k}{2} (\xi^2 + \eta^2)_{max} \quad (7.8)$$

The field at the *Fraunhofer region* or *far field* can be expressed directly as the Fourier transform of the aperture, by employing (7.8) into (7.7):

$$U(x, y, z) = \frac{e^{jkz}}{j\lambda z} e^{j\frac{k}{2z}(x^2+y^2)} \iint_{-\infty}^{\infty} U(\xi, \eta, 0) e^{-j\frac{2\pi}{\lambda z}(x\xi+y\eta)} d\xi d\eta \quad (7.9)$$

Where the expression will be evaluated at the following *spatial frequencies*:

$$f_x = \frac{x}{\lambda z} \quad (7.10.1)$$

$$f_y = \frac{y}{\lambda z} \quad (7.10.2)$$

The algorithm will be implemented in MATLAB. It will use the Fraunhofer approximation always that the distance between planes meets the restrictions to use it. In case not, Fresnel expression will be employed.

7.2. Device model

Once the theoretical basis has been defined, the aperture function will be set. A gaussian beam will impact over the active zone of the cells. The active zone will follow a model where different values of intensity and phase will be associated even inside of each electrode.

Three conceptual zones will be created. The first one will correspond to the interpixel (Figure 38, inter-pixel). The second one corresponds to the border electrodes (Figure 38, electrodes A and E), that will be affected by other zones electric field. The third one will be composed by the inner subpixels (Figure 38, subpixels B, C, and D), that will not be impacted by border effects and will maintain a regular phase distribution.

In order to explain the model, it will be supposed that the device has a fill ratio of 5/6. One subpixel will correspond to the interpixel and the other 5 will be used to emulate the phase variation over the electrode. A graphical representation for two electrodes is shown at Figure 38.

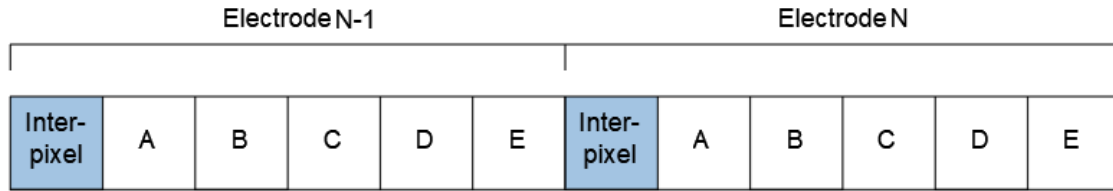


Figure 38: Electrodes model. Example for fill ratio of 5/6.

The phase variation is calculated as:

$$A(\phi) (\text{Electrode } n) = \begin{cases} \text{Interpixel} = R * \text{Phase}(N - 1) + (1 - R) * \text{Phase}(N - 1) \\ A = Q * \text{Phase}(N) + (1 - Q) * \text{Phase}(N - 1) \\ B = \text{Phase}(N) \\ C = \text{Phase}(N) \\ D = \text{Phase}(N) \\ E = Q * \text{Phase}(N) + (1 - Q) * \text{Phase}(N + 1) \end{cases}$$

The approximation was built in order to emulate the imperfections of the cells and the interpixel influence. Being discrete elements over which it has been defined specific values of voltage, it could be expected that the adjacent zones have an impact among them.

Fringe effects, that can be understood as the impact on the phase of two continuous electrodes where the phase reset from 2π to 0, will be also taken into account.

$$A(\phi_{\text{Fringe pixels}}) (\text{Electrode } n) = \begin{cases} D = F1 * \text{Phase}(N) \\ E = F2 * \text{Phase}(N) + F3 * \text{Phase}(N + 1) \end{cases}$$

This expression will model basically the same effect than the previous one but penalizing the bigger phase jump.

Setting the weights to $R=0.5$, $Q=0.8$ for a fill factor equals to 3/4 (subpixels B, C, D at explained model will be reduced to one); and adding a factor to reduce the transmittance of the interpixel to 75% (this is the zone where the ITO layer was erased), a phase profile has been obtained for topology 12 and presented at Figure 39.

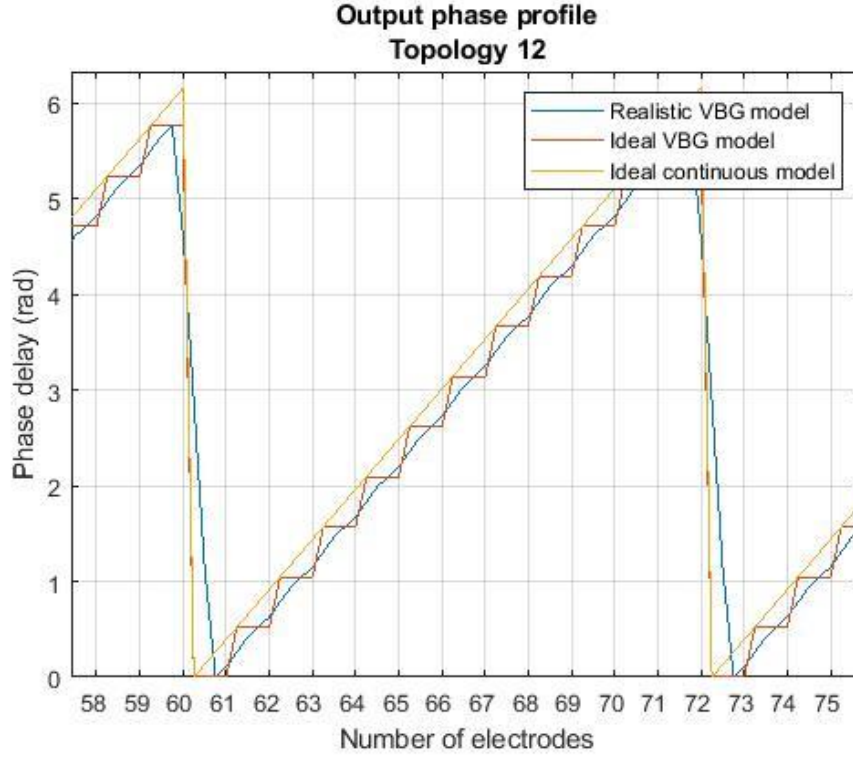


Figure 39: Electrodes phase distribution in an ideal case and the modelled VBG schemes.

Figure 39 help to compare the ideal situation for a device implementing an ideal VBG schema, a realistic approximation to it, and a continuous phase distribution.

It is important to note that fringing effects, as they have been modelled, give rise to erratic phase distributions that destroy the device operation at the simulation including a performance penalty too high. It is needed to develop a better model that allows to control its impact. From this point ahead, they will not be taken into consideration and the continuous electrodes that suffer a phase reset will be modelled as any other one.

7.3. Diffraction efficiency

The diffraction efficiency of the grating will give the power ratio between the order of interest (deviated beam) and the total power present at the image plane.

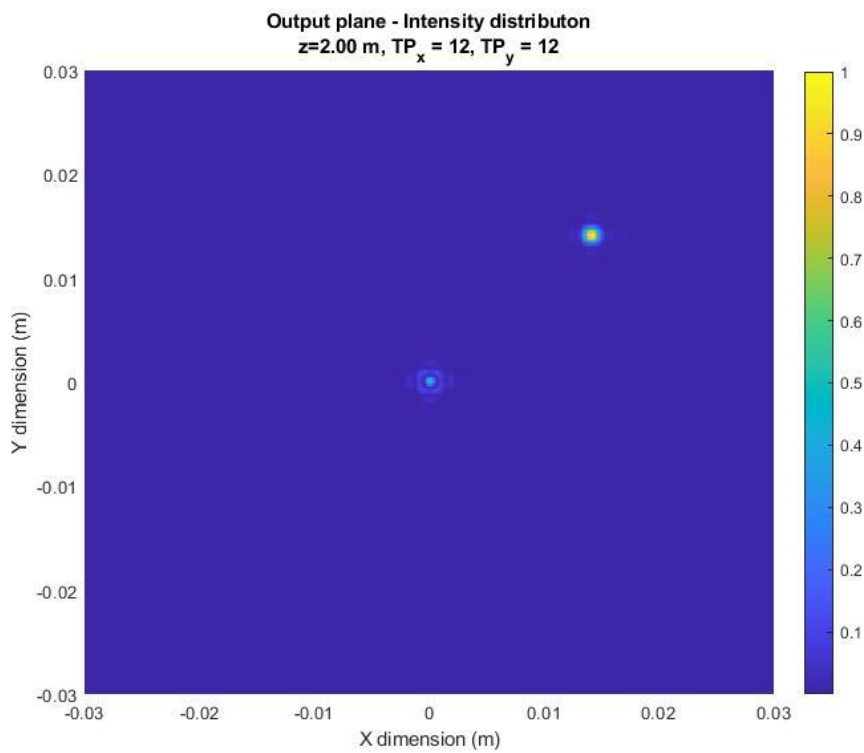
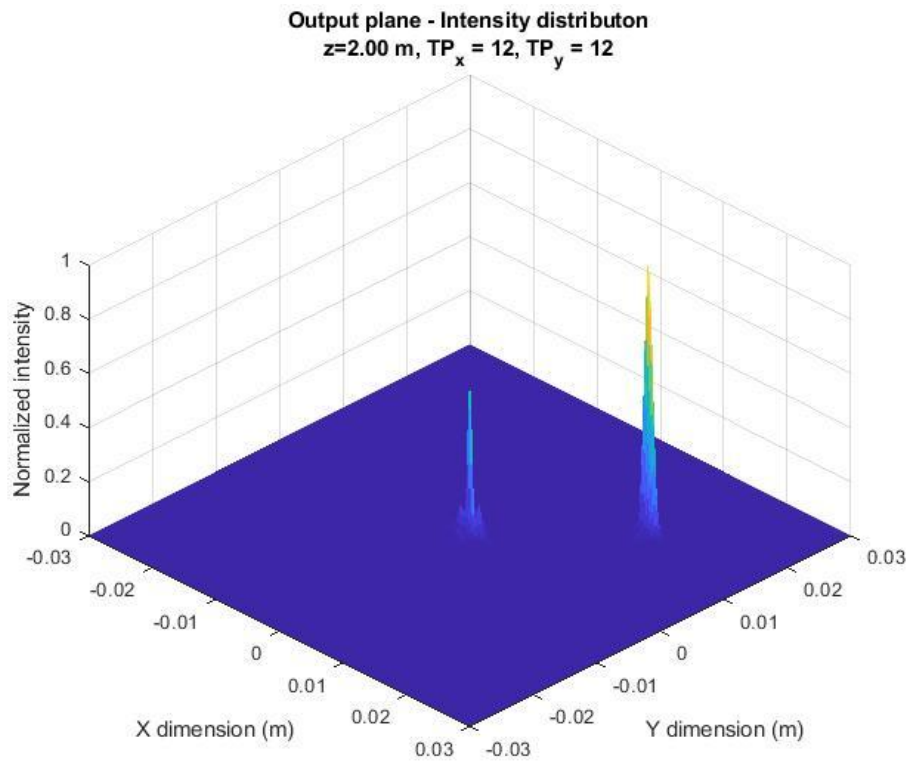
To build the simulation, the incident light will be assumed to follow a gaussian profile, normalized in terms of power, and centered at the active zone with a standard deviation of 0,5 mm. The grating efficiency will be calculated at a distance of 2 m with a resolution of 2^{12} pixels per dimension, which give rise to a plane of 2^{24} pixels. All the calculations will be made taking the number of pixels (points of simulation) as relative unit. The conversion between distance units and pixels is related through:

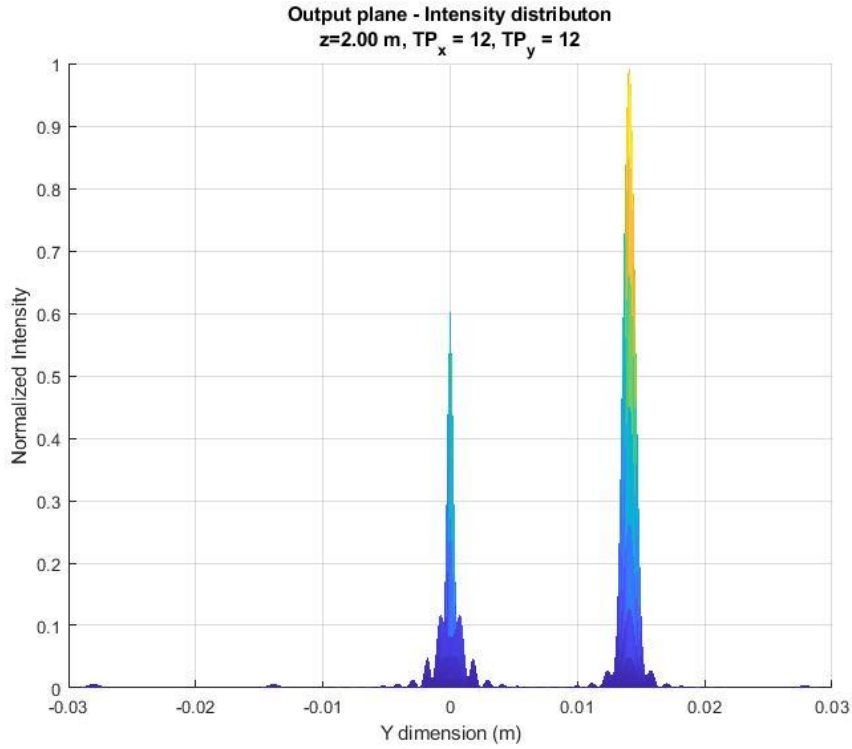
$$\delta_{in} = \frac{Pitch_{AZ}}{N_{sub}} = \frac{W_{in}}{N_{sub} \cdot N_{pix}} \quad (7.11)$$

$$\delta_{out} = \frac{\lambda \cdot z}{\delta_{in} \cdot N_{sub} \cdot N_{pix}} = \frac{\lambda \cdot z}{W_{in}} \quad (7.12)$$

Where $Pitch_{AZ}$ is the length of one pixel, N_{sub} the number of subdivisions for a pixel, N_{pix} the number of pixels in the plane, W_{in} the width of the input plane, λ the wavelength of the input

beam and z the distance between planes. Given this information, the diffraction pattern will be presented. As an example, Figure 40 shows the output of the simulation for a single run, with 12th topology for both dimensions.





(c)

Figure 40: Diffraction pattern for topology (+12,+12). (a) 3D, (b) 2D XY-plane, (c) 2D YZ-plane.

Having a 75% fill ratio leads to a significant leak of power that will not be steered. The 0th order is relatively large if compared to the 1st order present at the right in Figure 40 (c). However, at low topologies as in this case, the magnitudes for any other orders are almost negligible. This phenomenon could be later seen at sections 8.2.1 and 8.3.1.

Once interpreted the axes in terms of distance, the angle is obtained straight forward as:

$$tg(\theta) = \frac{\Delta r}{z} \quad (7.13)$$

Figure 41 shows the efficiency map obtained combining all the possible integer topologies ranging from -72 to 72. The module in charge of this calculation (see Annex 10.4.5 for details) will pick the 1st order peak and integrate its power to compare it with the total power present at the plane. The concept for efficiency employed at this work will not consider additional penalties as the ones generated by the opacity of the interpixel, and therefore, it cannot be understood as an insertion loss parameter.

As the angle increases, the beam expands slightly and increases its ellipticity. The integration radio is modified, increasing with the topologies.

High values of efficiency in topologies around zero have to do with the fact that the algorithm is not able to discriminate properly between the 0th order and the 1st order when both are too next when taking this approach.

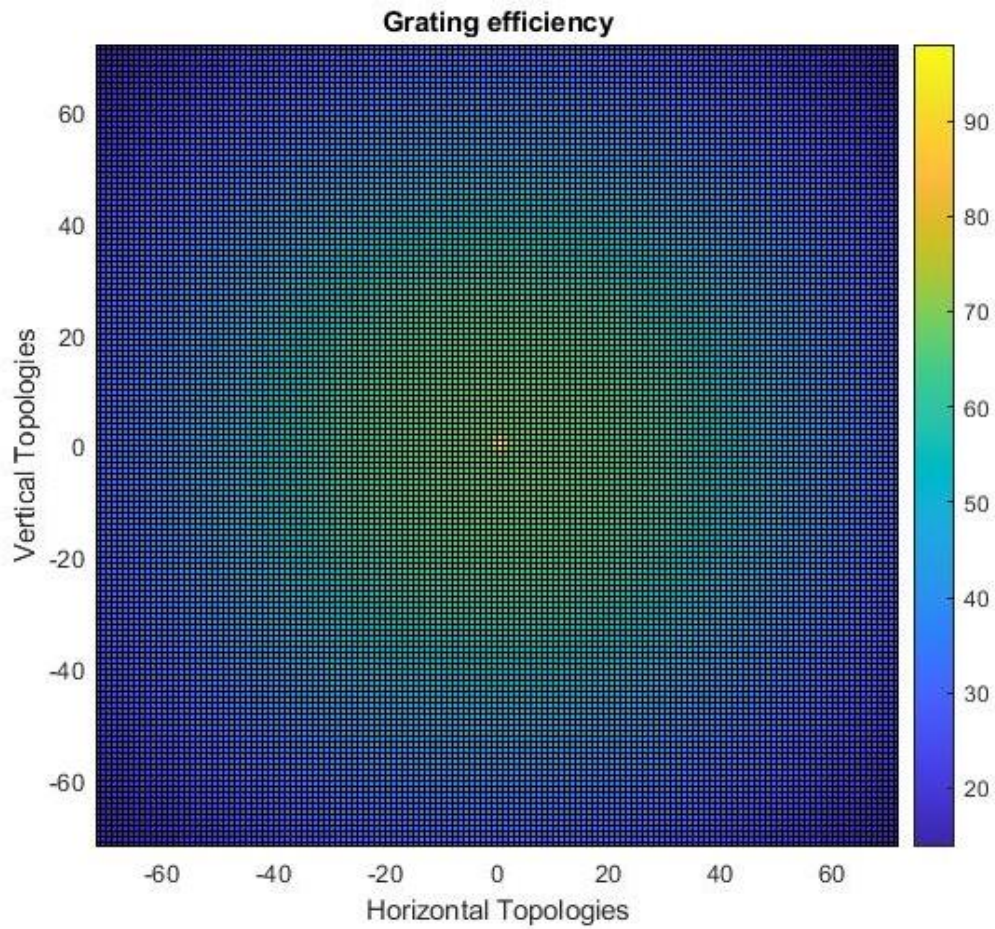


Figure 41: 2D grating efficiency for complete device (2 cells).

Figure 42 shows the symmetry of the system in a contour plot to clarify this fact. The penalty induced is directly proportional to the steered angle, creating a circular pattern with center at 0th topology or 0°.

The equivalent efficiency for a full device will be no less than the product of each one separately. The distribution of efficiency does follow a pseudo-parabolic distribution, which is related to the squared term of the loss.

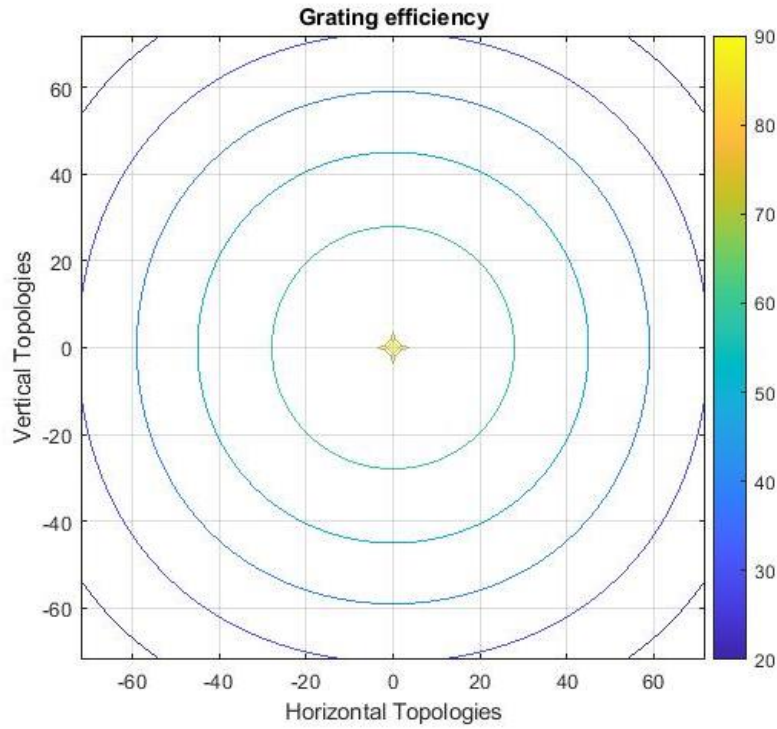


Figure 42: Grating efficiency (2 cells) contour.

The performance of the device drops critically as higher topologies are reached. Figure 43 shows the cross-section for one cell working fixed at 0th, 36th and 72nd topology, and the other one from -72nd to +72nd. It is important to note that being at 0th topology does have an impact on the grating efficiency, as it has been defined zones with limited transparency for the interpixel that create diffraction patterns. That is the reason why, although the majority of the power is situated at the center of the plane, the efficiency does not reach a value of 100%.

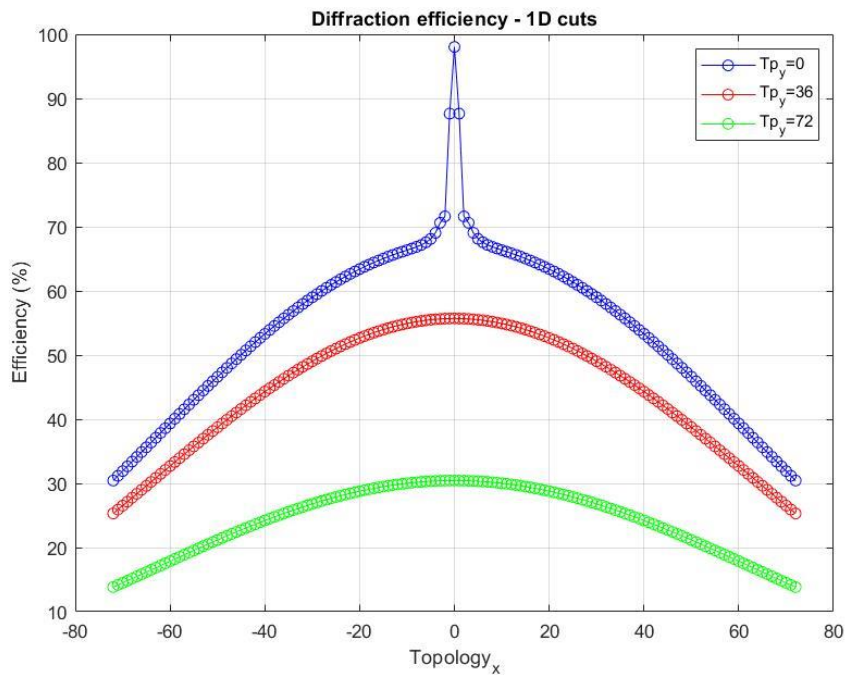


Figure 43: Grating efficiency (2 cells) cuts.

7.4. Steering angle

The deviation angle obtained with the grating could be expressed through:

$$\sin \theta = \frac{\lambda}{\Delta} \quad (7.14)$$

Being θ the angle, λ the wavelength of the input beam, and Δ the length of the phase period. Making use of the efficiency maps obtained previously and tracking the position of the deviated beam, the angle of deviation obtained through the MATLAB simulation can be compared to the one expected theoretically for an ideal device.

Figure 44 will compare the values obtained at the simulation by tracking the 1st order beam, to the theoretical ideal expression (7.14).

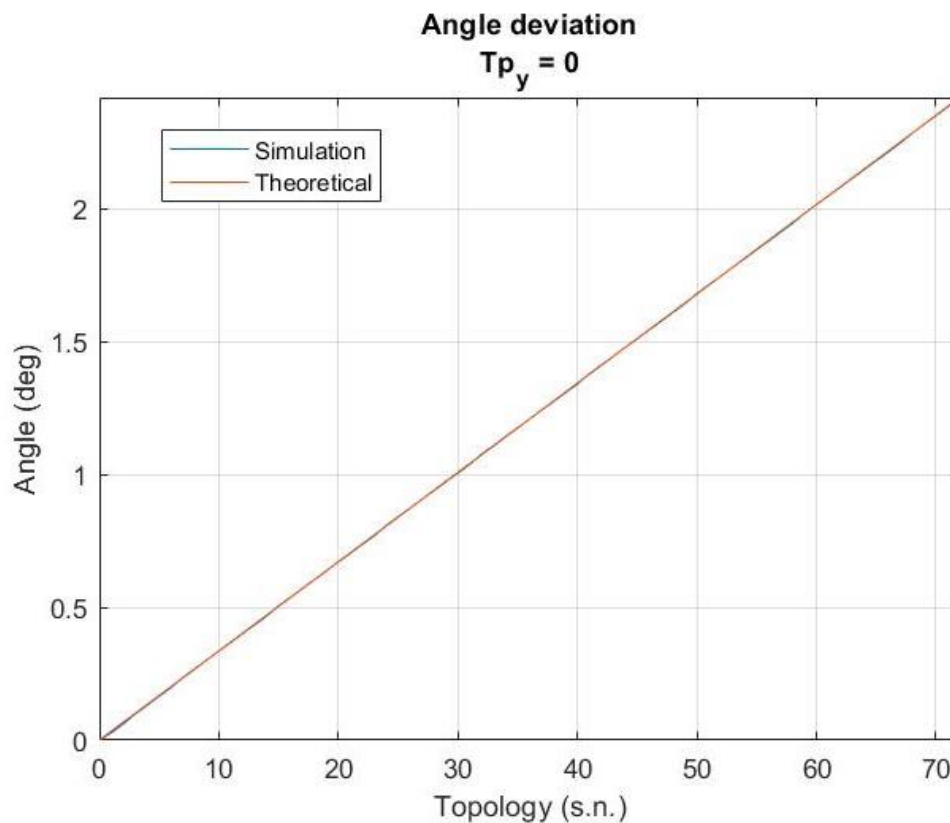


Figure 44: Angle of deflection simulated and calculated analytically.

The simulation values from the model used fit almost perfectly with the theoretical values. Checking the result obtained, with one cell not deviating the beam (0th topology), a maximum angle of steering of $\pm 2.42^\circ$ can be obtained from the center of the plane.

For both cells working in order to give the maximum phase delay ($\pm 72^{\text{nd}}$ topology), the maximum steering angle could be seen at the diagonals, $\pm 3.42^\circ$. Figure 45 will present the combined map of deflection.

As a measure of convenience to determine the steering angle, at a 50% of efficiency (around an accumulated topology of ± 45) an angle of $\pm 1.51^\circ$ is obtained.

The angle follows a linear distribution as expected. Checking the expression for a VBG scheme shown at section 3.3, the deflected angle will be inversely proportional to the length of the period where the 0 to 2π phase shift occurs.

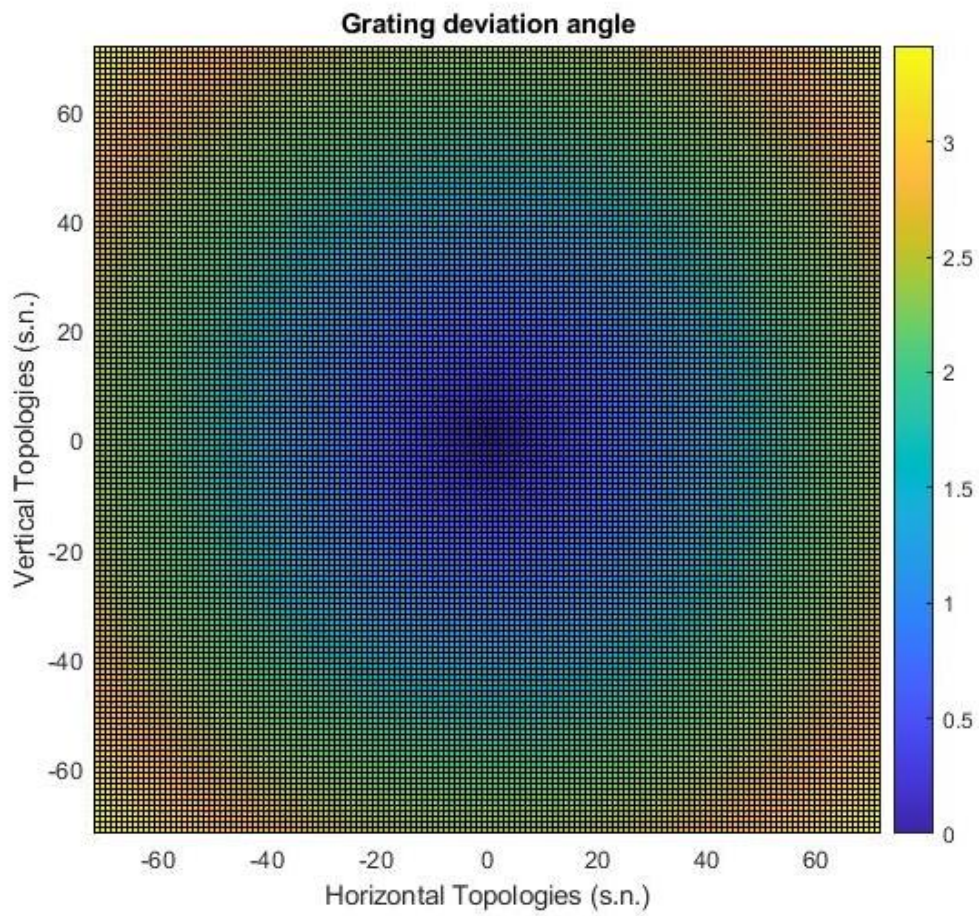


Figure 45: Deviation angle map.

Summarizing both results into a single representation, at Figure 46 is presented the map of diffraction efficiency versus the angle of deflection in each one of the dimensions.

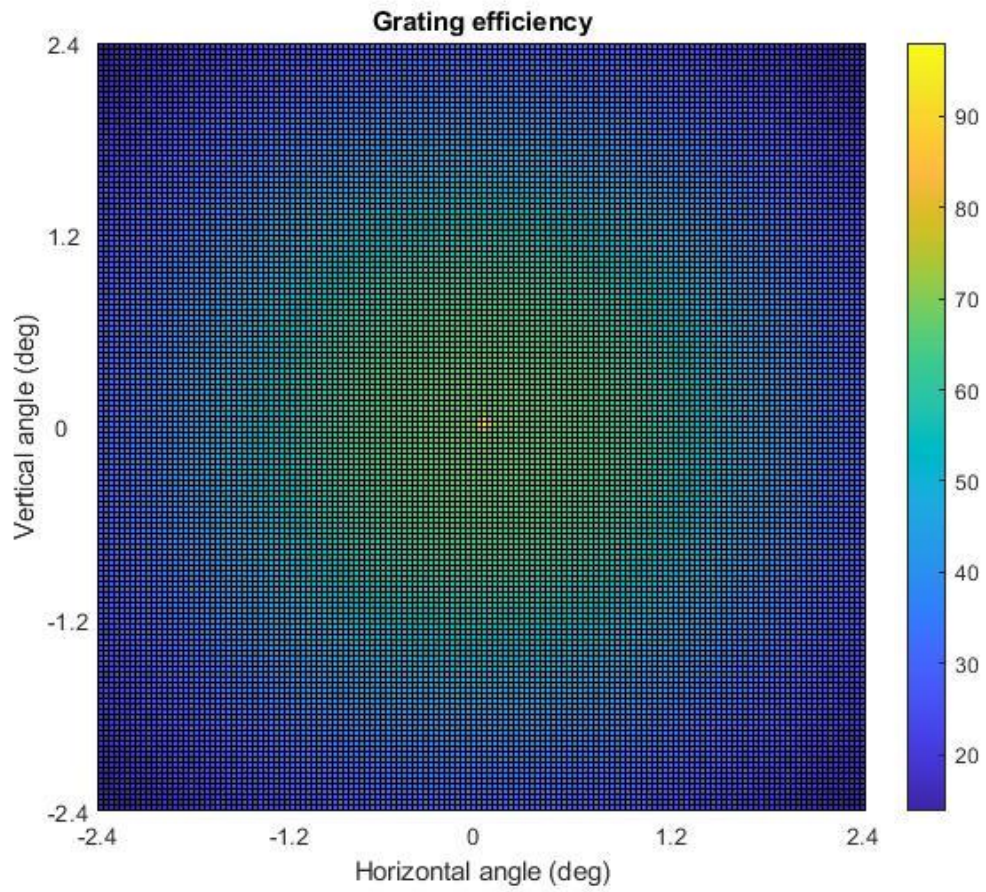


Figure 46: Diffraction efficiency as a function of the angle of deflection.

8. Results

The results obtained with the final device will be discussed here. A comparison against the values reflected by the simulation will be done in order to determine the validity of the model developed and the performance itself from the device.

8.1. Procedure

The steering device will be tested both with single cells and with two cells cascaded. For the last case, one of them will be reversed as it has been previously detailed in this work (to gain control over the perpendicular dimension from the first cell).

In this case, the attenuator and the polarizers will be excluded as the desired output is the diffraction patterns obtained when steering. A grided sheet will be installed at a known distance to measure the angle from the LC-OPA. Figure 47 will show the set-up employed.

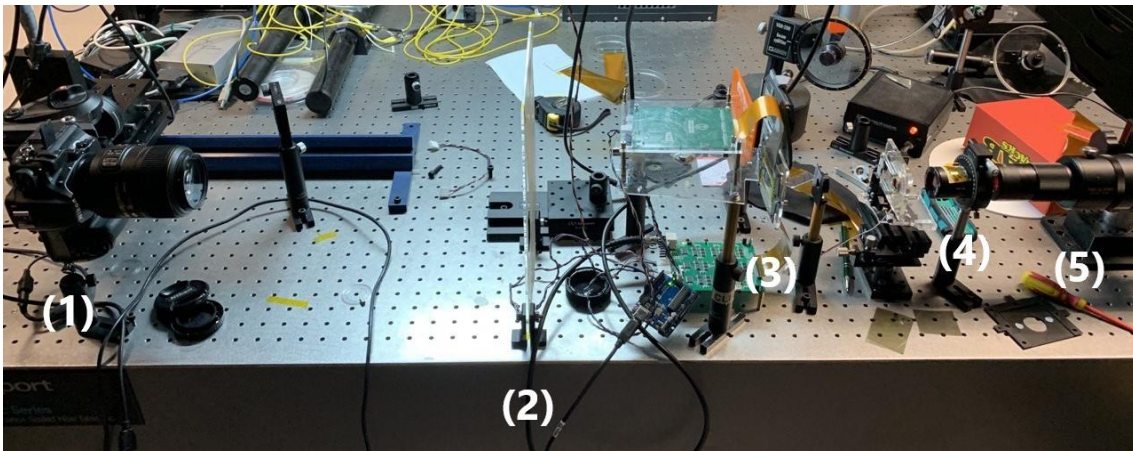


Figure 47: Results set-up.

The chain presented at Figure 47 is:

1. Camera.
2. Grided sheet.
3. LC-OPA.
4. 90° polarizer.
5. He-Ne laser (633 nm).

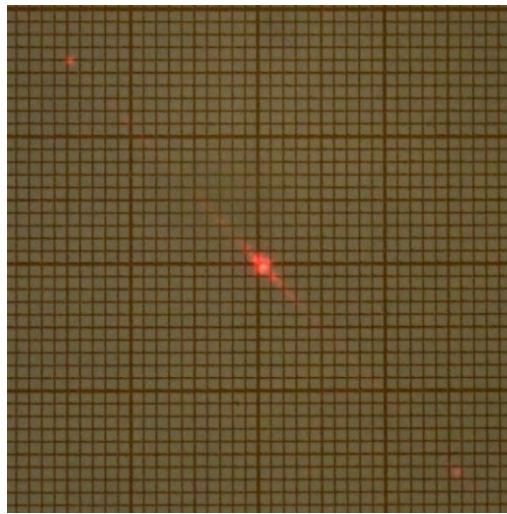
A LabVIEW routine used this time will allow to charge the desired topologies taking as input the parameters from the exponential model fitting. Images at this step first result will be taken manually. Additional details about the routine could be found at Annex 10.3.4. It will call the sub routine previously used at Chapter 6 (Annex 10.3.2) to generate the electrode levels.

8.2. 1D device results

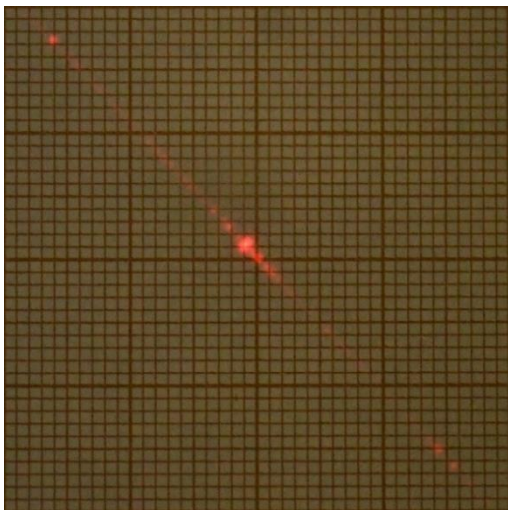
At this section, “Sample 5” will be used to obtain the results for a 1D steering device. It will be later included at the complete device with “Sample 7”.

8.2.1. Diffraction pattern

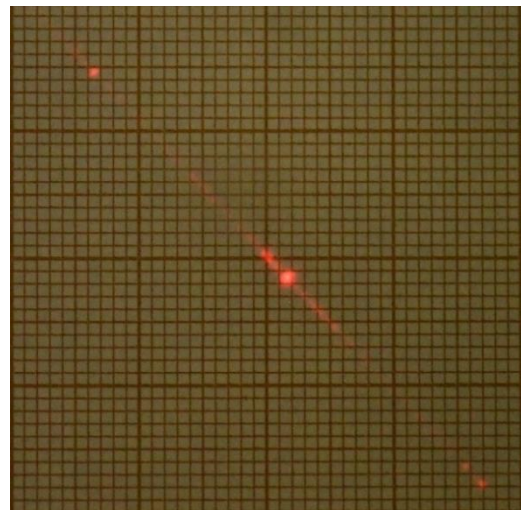
Figure 48 shows the diffraction pattern obtained for topologies 0, ± 12 , ± 36 and ± 72 . With the set-up used, positive topologies will move the beam to the left, and negative ones to the right.



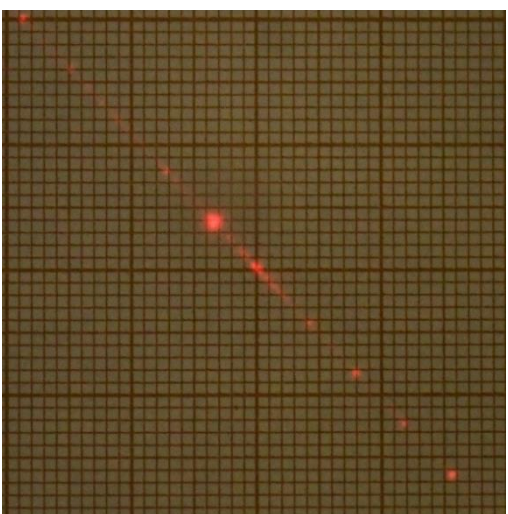
(a)



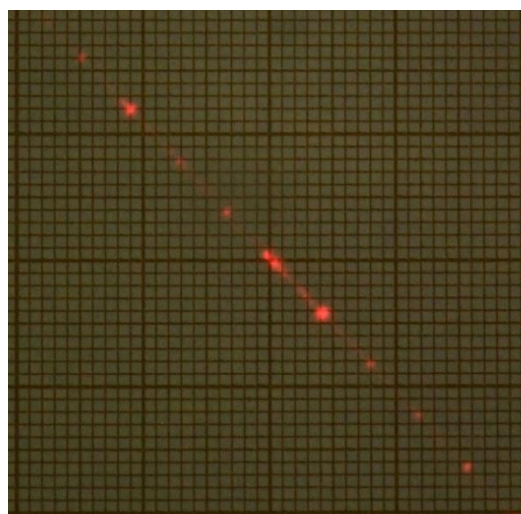
(b)



(c)



(d)



(e)

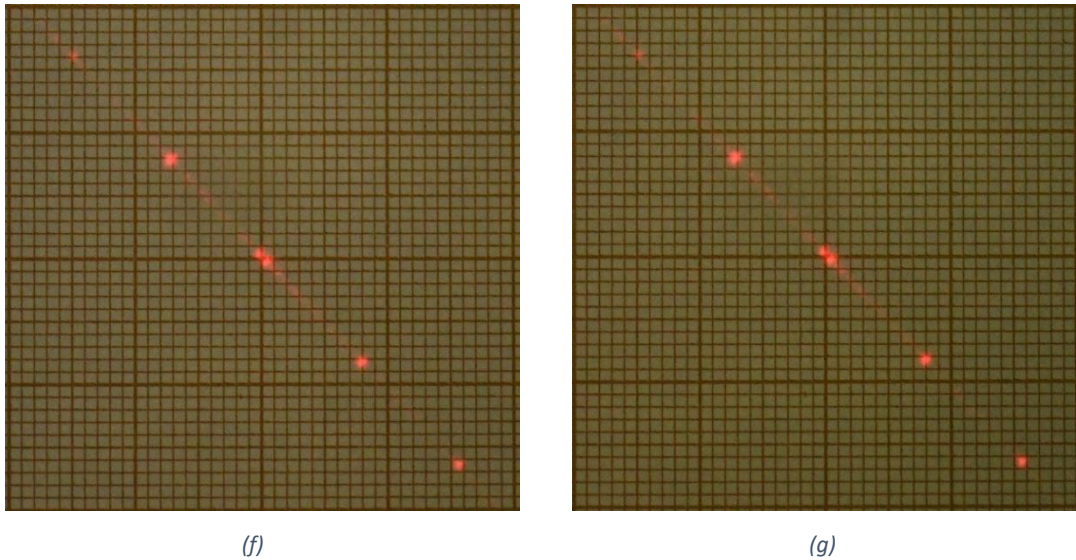


Figure 48: Steered beam with "Sample 5". (a) TP+0, (b) TP+12, (c) TP-12, (d) TP+36, (e) TP-36, (f) TP+72, (g) TP-72.

The high power values obtained at the 0th order, or central peak, confirm the difficulties of the manufacturing process. Some reasons, in decreasing order of importance, that could affect to increase the power at undesired orders could be:

- The **fill factor**. At the interpixel zones, no electric field is being driven, and thus, polarizing the LC as it should. Apart from its impact on the phase distribution, they are not completely opaque. Its effect will increase as the fill ratio decreases. For the device, the fill factor must be around 2/3.
- The **alignment layer**. For some of the cells manufactured, the thickness of the polyimide layer varied along the active zone. It could have an impact on the molecules alignment and the way they are reacting to the input electric fields.
- The **electronic driver**. The PCBs used to implement the driver depend on clock synchronization between the TLCs. Each 24 electrodes, a pattern could be appreciated where the field among the last and first electrode of two different TLCs can be summed destructively, giving an optical effect that the interpixel zone is much greater at it. As explained above at the fill factor point, these uncontrolled areas could be letting part of the light cross the device without steering it.
- The **exponential fit**. Creating an exponential model to describe the relationship between the induced phase and the applied voltage is a compromise between simplicity and accuracy. It might be expected some behavior driven a specific voltage that is wrong due to the approximation.

8.2.2. Steering angle

For topology ± 72 , at Figure 48 (f) and Figure 48 (g), taking into account that the grided sheet is at 27.5 cm and each hard marked square is 1 cm wide (having the smaller one a side 1 mm long) the beam is deviated around $\pm 2.35^\circ$ (around 8 small squares). This corroborate the values obtained at either the calculations made directly from the analytical theory solutions that were found at bibliography, and the ones from modeling the device and employing the Fresnel diffraction method.

It is important to note the ability to stablish non-integer topologies. Through the interpolation of the phase profile for the discrete elements, a quasi-continuous device could be reached, in terms of phase granularity.

The minimum angle step that could be taken will depend on the finesse at the characterization process. It will be directly related to the minimum phase step that could be used at the cell electrodes. Sampling a 0 to 2π phase shift with more points could be obtained either by increasing the bits of the electronic driver to express the PWM cycle (direct solution) or lengthen the curves of phase delay for a given driven voltage (indirect solution), so that a larger part of the driver range could be used to characterize one phase shift.

Figure 36 at section 6.2 shows how is being employed only a 35% of the available range. Lengthen the curve could be achieved for example employing smaller diameter spacers, that will give rise to reduce the optical path and the number of phase shifts that occur at the LC layer.

For the cell that is being discussed at this results section, "Sample 5" was calibrated between 1090 and 2350 (0 to 2π phase shift) out of 4096 total bits. It can be expected a minimum angle of deflection around 0.002° , by dividing the maximum angle of deflection by the total bits that are able to sample it.

8.2.3. Diffraction efficiency

It can be easily seen that the diffraction efficiency is better for smaller angles. It is important to recall that the functionality of analogue or continuous objects is being emulated with 'discrete' elements. As the number of topologies increase, the resolution of each of the saw-teeth decrease, giving rise to a loss of power on the peak of interest. Different illuminated points could be seen at the diffraction orders of the grating, getting brighter relatively as the resolution decrease, where the different wavefronts from each one of the teeth sum coherently³⁶. This could be checked qualitatively at Figure 48.

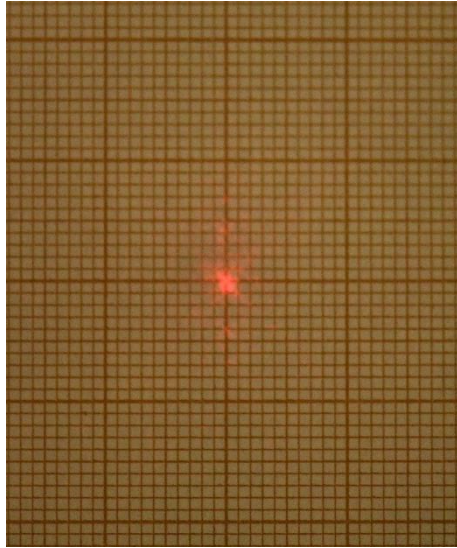
Due to technical problems, it was impossible to obtain the quantitative results in time. It will remain as a future line for this project.

8.3. 2D device results.

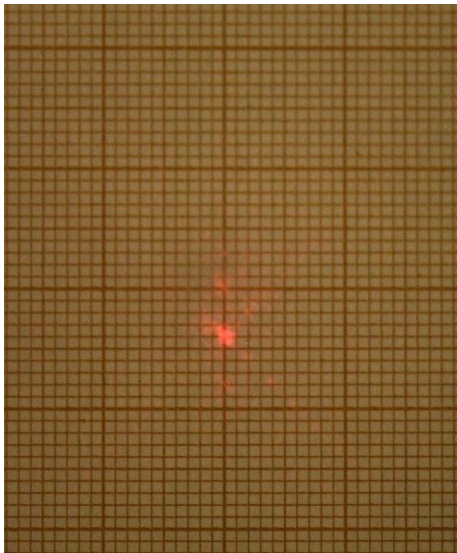
The 2D beam steerer discussed at this section will be composed by "Sample 5" and "Sample7". An image of the device was shown at Figure 32.

8.3.1. Diffraction pattern

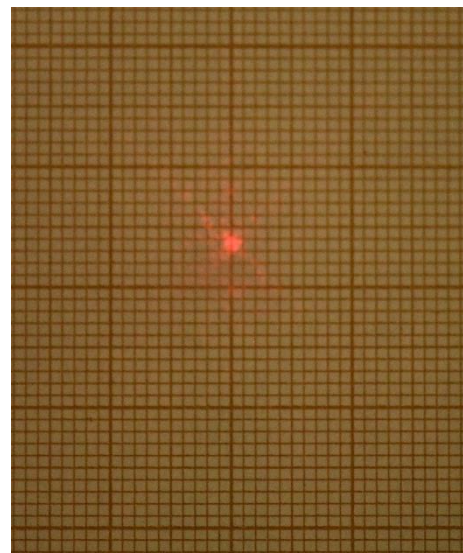
Figure 49 shows the diffraction pattern obtained for 2D beam steering. It has been obtained with both cells working at the same topology, with the grided sheet at 38 cm.



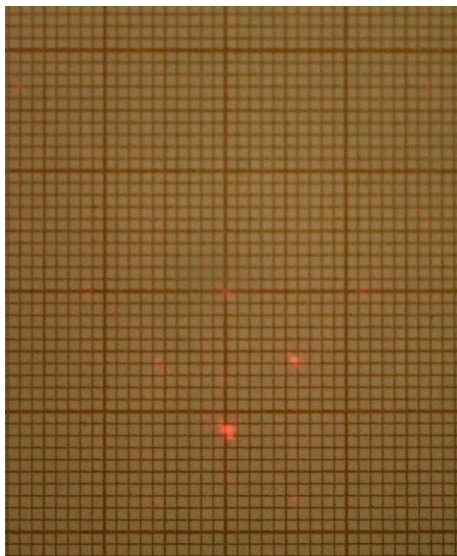
(a)



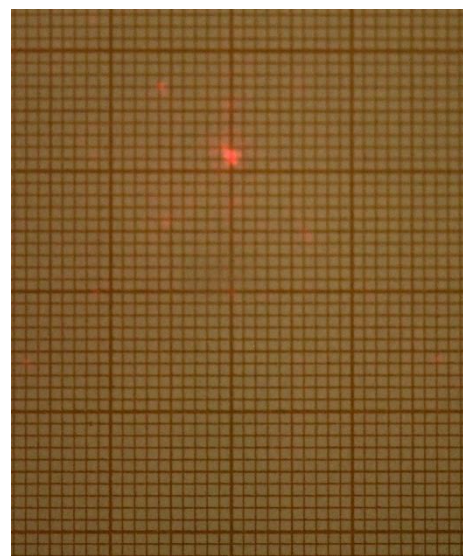
(b)



(c)



(d)



(e)

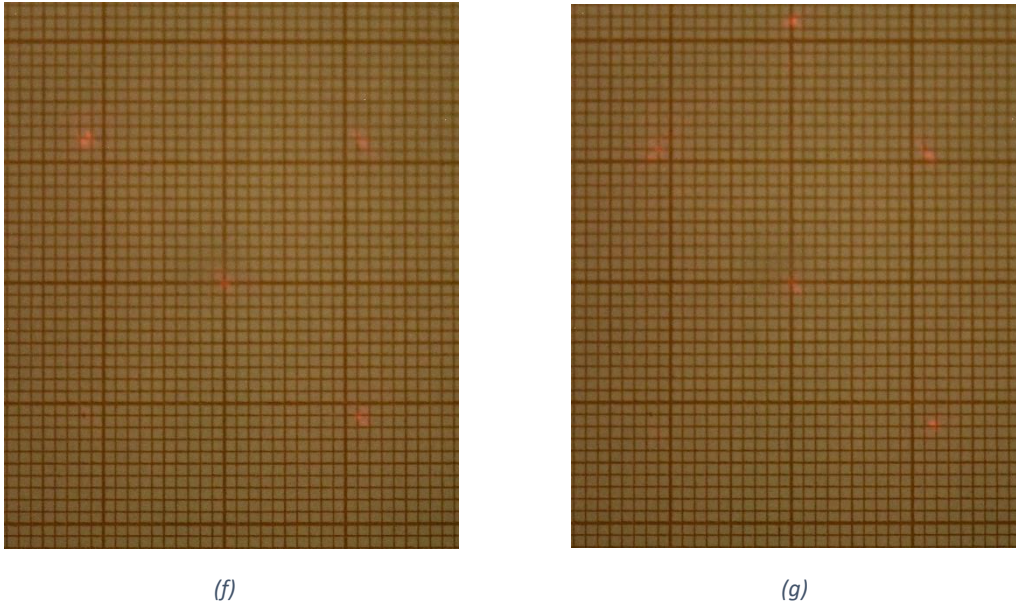


Figure 49: 2D Steered beam with “Sample 5” and “Sample 7”. (a) TP +0, (b) TP +12, (c) TP -12, (d) TP +36, (e) TP -36, (f) TP +72, (g) TP -72.

It can be seen a high impact on the 2D diffraction pattern in comparison to the one in 1D section (Figure 48). The combined fill factor has given rise to a decay of the output intensity that can be appreciated if compared to the 1D device results.

During the obtention of the diffraction patterns for the 2D device, the electronic driver showed an erratic behavior turning off randomly bins of 24 continuous electrodes, which could have altered the results.

8.3.2. Steering angle

The maximum deviated angle for a squared area of deviation will be located at the end of the diagonals. Checking the points situated topology ± 72 at Figure 49 (f) and Figure 49 (g), the order of interest is around 22 mm far from the center. The beam has been deviated around $3,31^\circ$.

The minimum angle will be determined by the minimum step at one of the single cells that compose the device. As already shown in section 8.2.2, the value for the 2D device will be 0.002°

8.3.3. Diffraction efficiency

As already explained in section 8.2.3, the values could not be obtained due to technical issues.

Table 2 present the results obtained at both sub-sections in a condensed way to clarify the final output of this work.

	Maximum angle ($^\circ$)	Minimum step ($^\circ$)	Fill factor (%)
1D device (Sample 5)	3.31	0.002	75
2D device (Samples 5 and 7)	2.35	0.002	56.75

Table 2: 1D and 2D device results.

9. Conclusions

The results obtained present a device suitable for deflecting a beam in free space propagation configurations. This proof of concept consolidates the idea of making use of this type of beam steerers for applications where mechanical solutions face inherent problems due to its nature, with appealing characteristics in terms of size, weight, and power. It has been managed to improve the maximum and minimum steering angle, with a reasonable efficiency for LC beam steerers. The fill-factor has been compromised for the 2D device, descending to a 56.75% due to manufacturing limitations.

With respect to the developed simulations, they have endorsed the values obtained with the manufactured device and have demonstrated being a good tool to test previously critical manufacturing parameters.

Being the performance of the device heavily impacted by the manufacturing process, it is expected to improve in terms of efficiency, maximum steering angle and minimum angle step. The procedures followed for manufacturing are not complex and could be easily perfected in a production chain.

9.1. Future lines

In order to improve the current design, some lines are proposed:

- **Reducing the fill factor.** Reducing the amount of non-transmission zone has a direct impact on the grating efficiency.
- **Reducing the active zone pitch.** There is a trade-off between the width of the electrodes at the interest zone and the fill ratio. If controlling properly the fill ratio is managed, the spatial resolution will increase and will allow to propose steeper phase profiles in the same space.
- **Studying different architectures to polarize the cell.** The discrete scheme employed could limit the performance of the cell due to fringe effects. If the manufacturing process allow diminishing the pitch at the active zone, the border effects will worsen.
- **Improve the electronic driver.** As in the case of the active zone granularity, improving the resolution at the electronic driver will allow to finer tunings for the voltage. Smaller steps at it will directly mean smaller available deflection angles.
- **Create a more suitable model for border effects.** The simulations where the fringe effects were taken into account did not work as expected. It is needed to develop a more suitable model to discern the effect of phase resets on continuous electrodes.
- **Obtain 1D and 2D steering efficiency curves.** Due to time limitations, this work did not present all the gathered information about the studied device. Failures at the electronic driver and the routines meant to calculate the efficiency curves impeded the device work properly during its obtention. Solving these issues will allow to get the efficiency curves versus the deflected angle, an extremely useful measurement.

10. Annex

10.1. Ethical, economic, social, and environmental aspects

10.1.1. Introduction

The aim of this work was proposing a beam steering device, with a high attention in terms of SWaP that could be taken as a viable option in the current industrial trends. Increasing the knowledge in this specific topic could give rise to an increase of performance of many of the current applications, which have been shown at Chapter 2, or allow its development.

Space applications will be of special interest the following decades and will suppose a jump ahead in terms of the human being development. Getting positioned in this explosion of a new era or helping to accelerate the process are targets that this work tries to aim at.

10.1.2. Relevant impacts related to the project description

Along this section, they will be presented the most relevant impacts that entails the realization of this project.

10.1.2.1. Electromagnetic radiation

The device has a certain precision when steering a beam. Depending on the application, it could be pointed to undesired places, being important to study the possible side-effects.

Electromagnetic radiation could alter the state of matter at high frequencies (ionizing waves) and modify the human DNA chains. This phenomenon is completely delimited by bibliography, and the harmful limits are well defined. Visible light, the domain under test when manufacturing this device, are frequencies far enough from ionizing ones.

However, the thermal effects must be considered. For now, the device does not allow large apertures or high efficiencies, but if manufacturing process improves it could give rise to potential problems.

10.1.2.2. Ethical content

Being conceptually a device for aiming to specific targets, its application at the military industry is direct. Again, as already explained at the previous segment, the manufacturing process is not sufficiently good to build high performance devices and make them worth to be chosen.

10.1.2.3. Privacy issues

In case that the beam steerer is used as an element of a communication chain, possible unsought receptions must be taken into account. Two main issues will be faced:

- Beam dispersion along the free-space propagation.
- High orders generated by the grating design.

Both cases must be solved by other elements of the chain, i.e., introducing robust coding schemes that impede the access to private information.

10.1.2.4. Environmental aspects

During the manufacturing of the beam steerer, different chemical products and materials that must be processed properly has been used. Taking care of the environment is a duty that concerns us all. It must be prepared a recycling plan either at the manufacturing points and at the end of the device life to avoid environmental damage, in agreement with current legislation.

On the other hand, being low weight and power devices will limit the energy waste in comparison to other beam steering approaches. This is a critical parameter specially for space applications.

10.1.3. Conclusions

The impact generated by this Master Thesis is limited as it has been seen. The device itself is completely harmless and allow the development, or improvement, of activities with high interest.

10.2. Economic budget

This section will explain the associated costs to produce this Master Thesis. They will be divided into two separate sections. The first one will comprise the cost related to the document and the preliminary study, and the second one the costs related to the device manufacturing.

It must be taken into account that some of the prizes included are an approximation to the real costs due to privacy reasons and the difficulty to delimit the specific usage for this project, specifically those related to the material employed at the dark and clean rooms. The cost of the labor force is assumed to include the public welfare fees, based on Spanish wage scales.

10.2.1. Document cost

At this section, the number of hours employed at the document redaction, and the material employed for it will be included.

Labor force

	Hours	Prize/hour	Total
Researcher #1	100	€ 15,00	€ 1.500,00

Material resources

	Prize	Used (in months)	Amortization (in years)	Total
Personal computer (software included)	€ 1.025,00	2	5	€ 34,17
Laser printer	€ 340,00	2	5	€ 11,33
Resources Total				€ 45,50

General costs	15 %	over Direct Costs	€ 231,83
Industrial benefit	6 %	over Direct and Indirect Costs	€ 106,64

Budget subtotal			€ 1.883,96
VAT		21 %	€ 395,63

TOTAL			€ 2.279,60
--------------	--	--	-------------------

10.2.2. Device manufacturing

At this segment, the costs related to the design, manufacturing, characterization, and simulation of the beam steerer will be included. For the steps of manufacturing and characterization, I received help from one of the researchers from the investigation group CEMDATIC, being included so at the economic budget.

Instrumentation and materials employed at the clean and dark room will be roughly estimated for the reasons presented above, in an attempt to generate a realistic budget estimation.

Labor force

	Hours	Prize/hour	Total
Researcher #1	300	€ 20,00	€ 6.000,00
Researcher #2	400	€ 15,00	€ 6.000,00

Material resources

	Prize	Used (in months)	Amortization (in years)	Total
Personal computer (software included)	€ 1.025,00	4	5	€ 68,33
Clean room instrumentation	€ 400.000,00	4	10	€ 13.333,33
Clean room material	€ 500,00	x	x	€ 500,00
Dark room instrumentation	€ 50.000,00	4	10	€ 1.666,67
Resources Total				€ 15.500,00

General costs	15%	over Direct Costs	€ 3.225,00
Industrial benefit	6%	over Direct and Indirect Costs	€ 1.483,50

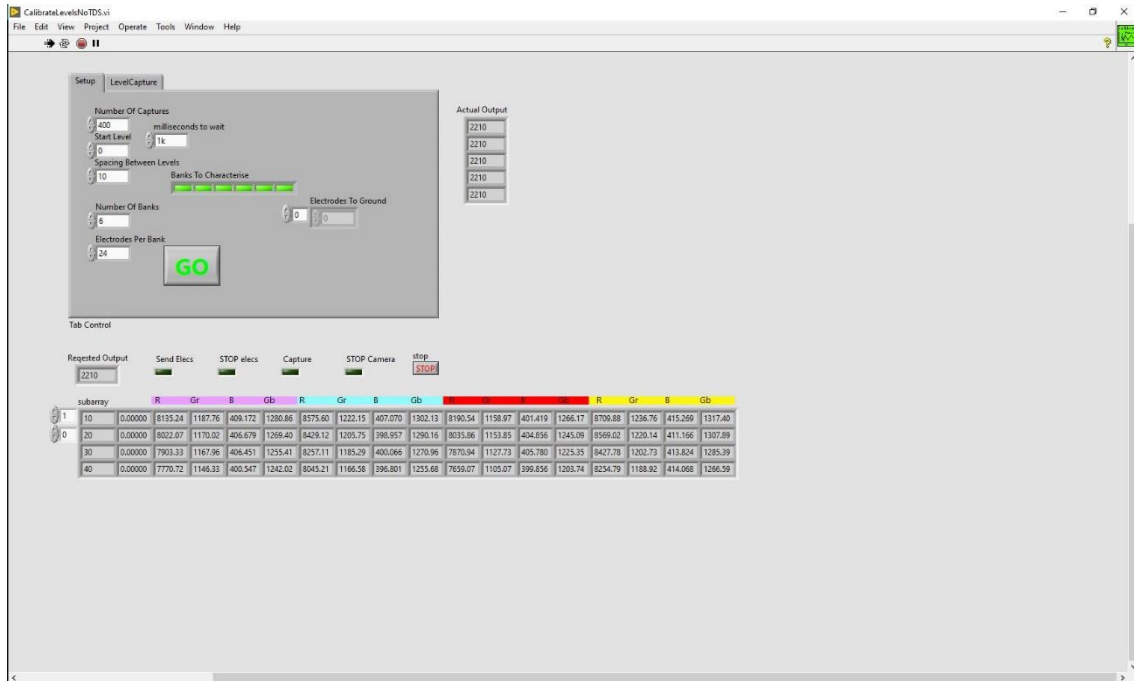
Budget subtotal			€ 26.208,50
VAT		21%	€ 5.503,79

TOTAL			€ 31.712,29
--------------	--	--	-------------

10.3. LabVIEW routines

This section will show briefly the LabVIEW routines employed to develop this Master Thesis. The authorship of this routines belongs exclusively to Morten Andreas Geday and Mario García de Blas, researchers at the Technical University of Madrid (CEMDATIC).

10.3.1. CalibrateLevelsNoTDS.vi

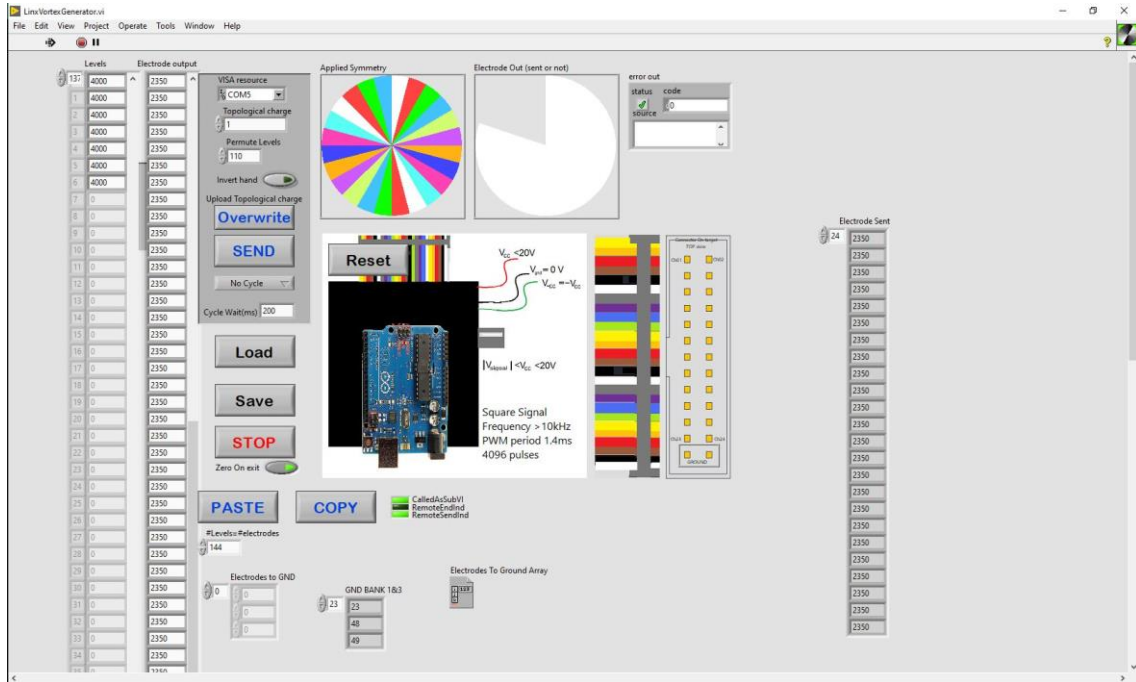


This module allows defining the interval of PWM values in terms of number of captures, step between them, and initial capture (in bits) value.

The routine was thought to be used with the same electronic driver but with different devices. It must be selected the number of TLCs employed (banks) at the PCBs. For a device with 144 electrodes, 6 banks (24 electrodes each TLC) are needed.

Activating this routine will trigger LinxVortexGenerator.vi and Nikon500Full.vi to obtain the values for light intensity at the PWM interval previously chosen. The data could be exported either as CSV format or directly into the clipboard.

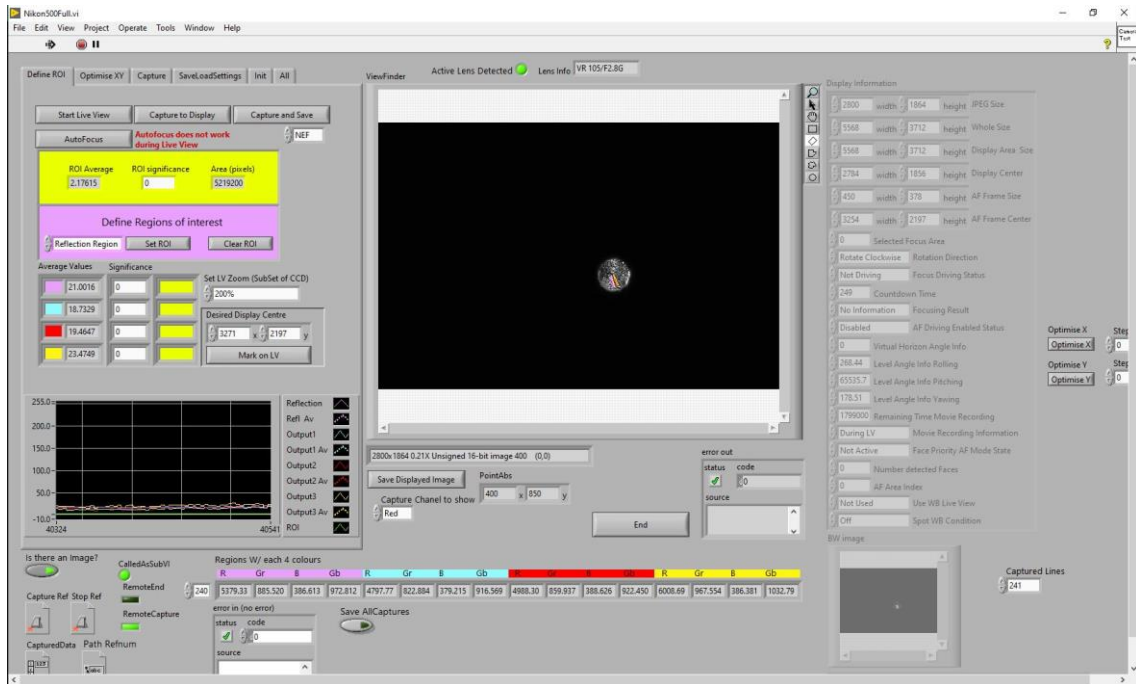
10.3.2. LinxVortexGenerator.vi



This module will charge the PWM value obtained from CalibrateLevelsNoTDS.vi and propagate it through all the electrodes.

Individually, it could be used to charge any desired scheme. It has a built-in structure to rotate electrodes with a specified cycle and a selector of topology, in case that it is desired to build a phase distribution with more resets without changing manually the values.

10.3.3. Nikon500Full.vi

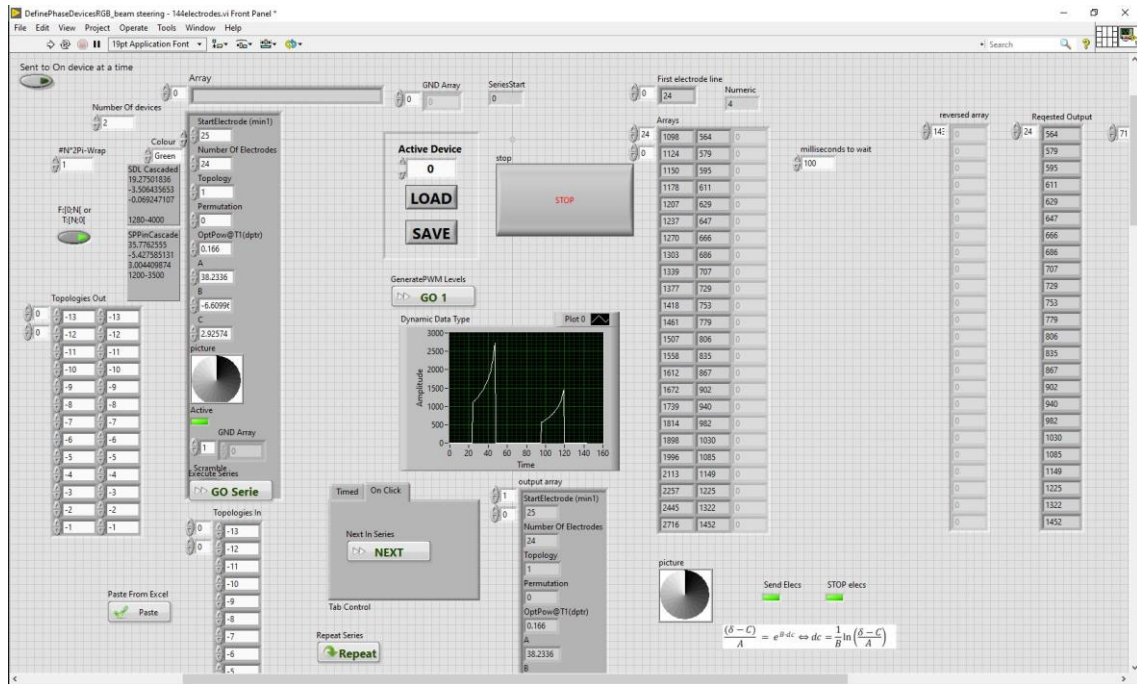


This module, as well as LinxVortexGenerator.vi, could be used independently or as a sub module for CalibrateLevelsNoTDS.vi. It will control the camera, a Nikon D500, directly from the

PC. Apart from modifying some relevant operation setting from the camera, the most relevant feature is the selection of Regions Of Interest (purple square at Figure X).

The intensity values, in a RGBG scheme, will be captured at those zones in order to compare them. This will be used to check that all the sections of the active zone behave similarly when it is applied the same voltage.

10.3.4. DefinePhaseDevicesRGB.vi



This routine can be used to control a complete device using as input the calibration values for the exponential approximation, and the desired topology. It will be in charge of delivering the voltage or phase profile adjusted to the characteristics of the cell.

10.4. MATLAB routines

This section will collect the code snippets used to obtain all the simulation results present at Chapter 7.

10.4.1. BeamSteering_Simulation.m

This module will be the main routine. The first section is used to do a preallocation of the parameters of the simulation. Three different methods or desired outputs are configured.

The first one will be used for simulating only one combination of topologies. It presents graphically the input and output planes and gives information about the angle deflected and efficiency obtained.

The other two will use a for loop to obtain general performance results from the device. It will be obtained from here for example the general maps of diffraction efficiency. The difference between the 2nd and 3rd method is the model they use for generating the input plane, being the 3rd one an ideal approximation and the 2nd one a realistic model.

```
%--- Beam Steering performance simulation
% Algorithm: Fresnel/Fraunhofer diffraction formula
% It has two execution methods. 1st one for single topology run and 2nd one
% prepared for arrays. Different plots are presented in each one
tic
clc
close all
clear all

%--- Parameters
% General
SIM_PARAMETERS.lambda = 633e-9; % Light wavelength [m]
SIM_PARAMETERS.k = 2*pi/SIM_PARAMETERS.lambda; % Wave number (m-1)
SIM_PARAMETERS.z = 2; % Distance between planes [m]

% Method 1
SIM_PARAMETERS.topologyX = 12;
SIM_PARAMETERS.topologyY = 12;

% Method 2
SIM_PARAMETERS.topologyX_array = [-72:72];
SIM_PARAMETERS.topologyY_array = [-72:72];

% Input plane - Cells
cell.nElectrodes = 144; % Number of electrodes at Active Zone
cell.electrodeSubdivision = 4; % Number of parts that form an electrode
cell.pitchAZ = 7.5e-6; % Electrode width at Active Zone (m)
cell.widthAZ = cell.pitchAZ * cell.nElectrodes; % Pixel width at Active Zone (m)
cell.Npix = cell.nElectrodes * cell.electrodeSubdivision; % Number of simulation pixels
cell.delta = cell.widthAZ / cell.Npix; %m/px

% Input plane - generic
% input_plane.W = 2e-3; % width of input plane [m]
input_plane.Nb = 12; % Bits to simulate input plane
input_plane.Npix = 2^input_plane.Nb; % Pixels of input plane (width)

input_plane.delta = cell.pitchAZ/cell.electrodeSubdivision; % m/px
```

```

input_plane.axis = [-input_plane.Npix/2:input_plane.Npix/2-1] * ...
    input_plane.delta; % Input axis (m)
[input_plane.x_mesh,input_plane.y_mesh] = meshgrid(input_plane.axis,input_plane.axis);
input_plane.W = input_plane.delta * cell.nElectrodes * cell.electrodeSubdivision;

% Input plane - Model for aperture
electrodeModel.Q = 0.8; % Set to 1 for all-equal
electrodeModel.R1 = 0.5; % 0.5 %Set to 0 for all-equal
electrodeModel.FE1 = 1; % Fringe Effect electrode D
electrodeModel.FE2 = 1; % Fringe Efecct electrode E - 1st factor
electrodeModel.FE3 = 0; % Fringe Efecct electrode E - 2nd factor
electrodeModel.QQ = 0.75; % Interpix intensity percentage
electrodeModel.SS = 1; % Intensity in the other electrodes

% Input plane - Gaussian Beam
beam.x0 = 0; % Center of beam coordinates (m)
beam.y0 = 0;
beam.sigmaX = 0.5e-3; % Standard Deviation (m)
beam.sigmaY = 0.5e-3;

%Output plane - generic
output_plane.delta = SIM_PARAMETERS.lambda*SIM_PARAMETERS.z / ...
    (input_plane.delta * input_plane.Npix); % m/px
output_plane.axis = [-input_plane.Npix/2:input_plane.Npix/2-1] * ...
    output_plane.delta; % Output axis (m)
[output_plane.x_mesh,output_plane.y_mesh] =
meshgrid(output_plane.axis,output_plane.axis);

% Selector
method = 1; % 1-Specific_model 2-Range_model 3-Specific_ideal

%--- Simulation: Beam steering

if method == 1
    disp('Realistic VBG model build selected - Individual run')

    % Obtain pixels from cells
    [cell.x_dim ideal_x] = getApertureLC_V2(SIM_PARAMETERS.topologyX, cell.nElectrodes,
cell.electrodeSubdivision, electrodeModel, 'off'); % Obtained phase (and intensity)
distribution for X cell in the map defined [N,N] - 1D
    [cell.y_dim ideal_y] = getApertureLC_V2(SIM_PARAMETERS.topologyY, cell.nElectrodes,
cell.electrodeSubdivision, electrodeModel, 'off'); % Obtained phase (and intensity)
distribution for Y cell in the map defined [N,N] - 1D
    cell.y_dim = transpose(cell.y_dim); % Y cell transpose to
simulate the other dimension

    % Obtain gaussian beam
    beam.map =
gaussianBeam2D(input_plane.x_mesh,input_plane.y_mesh,beam.x0,beam.y0,beam.sigmaX,beam.si
gmaY, 'off');

    % Adapt cells to simulation window
    limit_down = length(beam.map)/2-length(cell.x_dim)/2+1;
    limit_up = length(beam.map)/2+length(cell.x_dim)/2;

    input_plane.E = beam.map;
    input_plane.E(limit_down:limit_up,limit_down:limit_up) =
beam.map(limit_down:limit_up,limit_down:limit_up) .*...

```

```

        cell.x_dim .* cell.y_dim;
    %     input_plane.E(limit_down:limit_up,limit_down:limit_up) =
beam.map(limit_down:limit_up,limit_down:limit_up) .*...
    %         ideal_x .* ideal_y;

    input_plane.I = abs(input_plane.E).^2;

    %Calculate diffraction pattern
    output_plane.fresnel.quadrature = exp(1i*SIM_PARAMETERS.k/(2*SIM_PARAMETERS.z).*...
        (input_plane.x_mesh.^2 + input_plane.y_mesh.^2));

    output_plane.fresnel.phaseFactor = exp(1i*SIM_PARAMETERS.k*SIM_PARAMETERS.z) * ...
        exp(1i*SIM_PARAMETERS.k*(output_plane.x_mesh.^2 +
output_plane.y_mesh.^2)/(2*SIM_PARAMETERS.z));

    output_plane.fresnel.amplitudeFactor = 1/(1i * SIM_PARAMETERS.lambda *
SIM_PARAMETERS.z);

    output_plane.E = fftshift(fft2(input_plane.E.*output_plane.fresnel.quadrature));
    output_plane.E = output_plane.E .*output_plane.fresnel.phaseFactor .*
output_plane.fresnel.amplitudeFactor;
    output_plane.I = abs(output_plane.E).^2;

    % Calculate efficiency of grating (relative power of point of interest)
    eff_ratio = getEfficiencyLC_V2(output_plane.I, SIM_PARAMETERS.topologyX,
SIM_PARAMETERS.topologyY);
    fprintf('Grating efficiency = %0.2f %%\n',eff_ratio);

    %     figure
    %     surf(input_plane.x_mesh, input_plane.y_mesh,
input_plane.I/max(max(input_plane.I)), 'LineStyle','none', 'FaceColor','interp');
    %     title(sprintf('Input plane - Intensity distributon\nz=0 m, TP_x = %i, TP_y =
%i',SIM_PARAMETERS.topologyX,SIM_PARAMETERS.topologyY))
    %     xlabel('X dimension (m)')
    %     ylabel('Y dimension (m)')

    figure

    surf(output_plane.x_mesh,output_plane.y_mesh, (output_plane.I/max(max(output_plane.I))), '
LineStyle','none')
    title(sprintf('Output plane - Intensity distributon\nz=%0.2f m, TP_x = %i, TP_y =
%i',SIM_PARAMETERS.z,SIM_PARAMETERS.topologyX,SIM_PARAMETERS.topologyY))
    xlabel('X dimension (m)')
    ylabel('Y dimension (m)')
    view(0,90)
    axis([-1 1 -1 1]*0.03)

elseif method == 2
    disp('Realistic VBG model build selected')

    result=zeros(length(SIM_PARAMETERS.topologyX_array),length(SIM_PARAMETERS.topologyY_arra
y));

    result_ang=zeros(length(SIM_PARAMETERS.topologyX_array),length(SIM_PARAMETERS.topologyY_
array));

```

```

for topologyX_counter = SIM_PARAMETERS.topologyX_array;
    fprintf('In progress... TP_X = %i\n',topologyX_counter);
    for topologyY_counter = SIM_PARAMETERS.topologyY_array;

        % Obtain pixels from cells
        [cell.x_dim ideal_x] = getApertureLC_V2(topologyX_counter, cell.nElectrodes,
        cell.electrodeSubdivision, electrodeModel, 'off'); % Obtained phase (and intensity)
        distribution for x cell in the map defined [N,N] - 1D
        [cell.y_dim ideal_y] = getApertureLC_V2(topologyY_counter, cell.nElectrodes,
        cell.electrodeSubdivision, electrodeModel, 'off'); % Obtained phase (and intensity)
        distribution for Y cell in the map defined [N,N] - 1D
        cell.y_dim = transpose(cell.y_dim); % Y cell transpose to
        simulate the other dimension

        % Obtain gaussian beam
        beam.map =
        gaussianBeam2D(input_plane.x_mesh,input_plane.y_mesh,beam.x0,beam.y0,beam.sigmaX,beam.si
        gmaY,'off');
        %beam.map = ones(input_plane.Npix, input_plane.Npix);

        % Adapt cells to simulation window
        limit_down = length(beam.map)/2-length(cell.x_dim)/2+1;
        limit_up = length(beam.map)/2+length(cell.x_dim)/2;

        input_plane.E = beam.map;
        input_plane.E(limit_down:limit_up,limit_down:limit_up) =
        beam.map(limit_down:limit_up,limit_down:limit_up) .*...
            cell.x_dim .* cell.y_dim;
        input_plane.I = abs(input_plane.E).^2;

        %Calculate diffraction pattern
        output_plane.fresnel.quadrature =
        exp(1i*SIM_PARAMETERS.k/(2*SIM_PARAMETERS.z).*...
            (input_plane.x_mesh.^2 + input_plane.y_mesh.^2));

        output_plane.fresnel.phaseFactor = exp(1i*SIM_PARAMETERS.k*SIM_PARAMETERS.z)
        * ...
            exp(1i*SIM_PARAMETERS.k*(output_plane.x_mesh.^2 +
            output_plane.y_mesh.^2)/(2*SIM_PARAMETERS.z));

        output_plane.fresnel.amplitudeFactor = 1/(1i * SIM_PARAMETERS.lambda *
        SIM_PARAMETERS.z);

        output_plane.E =
        fftshift(fft2(input_plane.E.*output_plane.fresnel.quadrature));
        output_plane.E = output_plane.E .*output_plane.fresnel.phaseFactor .*
        output_plane.fresnel.amplitudeFactor;
        output_plane.I = abs(output_plane.E).^2;

        % calculate efficiency of grating (relative power of point of interest)
        eff_ratio = getEfficiencyLC_V2(output_plane.I,topologyX_counter,
        topologyY_counter);
        result(SIM_PARAMETERS.topologyX_array == topologyX_counter,
        SIM_PARAMETERS.topologyY_array == topologyY_counter) = eff_ratio;

        % Calculate angle of diffraction (between 0th and 1st order)
        measuredAngle = getAngleLC(topologyX_counter,topologyY_counter,

```

```

output_plane.I, output_plane.axis, SIM_PARAMETERS.z);
    result_ang(SIM_PARAMETERS.topologyX_array == topologyX_counter,
SIM_PARAMETERS.topologyY_array == topologyY_counter) = measuredAngle;
    end
end

%Plotting
if length(SIM_PARAMETERS.topologyX_array) == 1 ||
length(SIM_PARAMETERS.topologyY_array) == 1
    figure
    plot(SIM_PARAMETERS.topologyX_array, result, 'o-b')
    title('Diffraction efficiency')
    legend(sprintf('Tp_y = %i', topologyY_counter))
    xlabel('Topology_x (s.n)')
    ylabel('Efficiency (%)')
    grid

    figure
    theoreticalAngle =
rad2deg(asin(SIM_PARAMETERS.lambda./(input_plane.w./SIM_PARAMETERS.topologyX_array)));
%asin(lambda/delta)
    plot(SIM_PARAMETERS.topologyX_array, result_ang);
    hold on
    plot(SIM_PARAMETERS.topologyX_array, theoreticalAngle);
    legend('Simulation', 'Theoretical');
    title(sprintf('Angle deviation\nTp_y = %i', topologyY_counter))
    ylabel('Angle (deg)')
    xlabel('Topology (s.n.)')
    hold off

    figure
    plot(SIM_PARAMETERS.topologyX_array, result_ang-theoreticalAngle')
    title(sprintf('Error at angle calculation\nTp_y = %i', topologyY_counter))
    ylabel('Angle (deg)')
    xlabel('Topology (s.n.)')

else
    figure
    title('Grating efficiency')
    surf(SIM_PARAMETERS.topologyX_array, SIM_PARAMETERS.topologyY_array, result)
    xlabel('Horizontal Topologies')
    ylabel('Vertical Topologies')
    zlabel('Efficiency (%)')

    figure
    title('Grating efficiency')
    surf(result_ang, result_ang, result)
    xlabel('Horizontal Angle (deg)')
    ylabel('Vertical Angle (deg)')
    zlabel('Efficiency (%)')

    figure
    surf(SIM_PARAMETERS.topologyX_array, SIM_PARAMETERS.topologyY_array, result_ang)
    title('Grating efficiency')
    xlabel('Horizontal Topologies (s.n.)')
    ylabel('Vertical Topologies (s.n.)')
    zlabel('Angle deviation(deg)')

```

```

end

elseif method == 3
    disp('Ideal VBG model build selected')

    result=zeros(length(SIM_PARAMETERS.topologyX_array),length(SIM_PARAMETERS.topologyY_
array));

    result_ang=zeros(length(SIM_PARAMETERS.topologyX_array),length(SIM_PARAMETERS.topologyY_
array));
    for topologyX_counter = SIM_PARAMETERS.topologyX_array;
        fprintf('In progress... TP_X = %i\n',topologyX_counter);
        for topologyY_counter = SIM_PARAMETERS.topologyY_array;

            % Obtain pixels from cells
            [cell.x_dim ideal_x] = getApertureLC_V2(topologyX_counter, cell.nElectrodes,
cell.electrodeSubdivision, electrodeModel, 'off'); % Obtained phase (and intensity)
distribution for X cell in the map defined [N,N] - 1D
            [cell.y_dim ideal_y] = getApertureLC_V2(topologyY_counter, cell.nElectrodes,
cell.electrodeSubdivision, electrodeModel, 'off'); % Obtained phase (and intensity)
distribution for Y cell in the map defined [N,N] - 1D

            cell.x_dim = ideal_x;
            cell.y_dim = ideal_y;

            cell.y_dim = transpose(cell.y_dim); % Y cell transpose to
simulate the other dimension

            % Obtain gaussian beam
            beam.map =
gaussianBeam2D(input_plane.x_mesh,input_plane.y_mesh,beam.x0,beam.y0,beam.sigmax,beam.si
gmay,'off');

            % Adapt cells to simulation window
            limit_down = length(beam.map)/2-length(cell.x_dim)/2+1;
            limit_up = length(beam.map)/2+length(cell.x_dim)/2;

            input_plane.E = beam.map;
            input_plane.E(limit_down:limit_up,limit_down:limit_up) =
beam.map(limit_down:limit_up,limit_down:limit_up) .*...
                cell.x_dim .* cell.y_dim;
            input_plane.I = abs(input_plane.E).^2;

            %Calculate diffraction pattern
            output_plane.fresnel.quadrature =
exp(1i*SIM_PARAMETERS.k/(2*SIM_PARAMETERS.z).*...
                (input_plane.x_mesh.^2 + input_plane.y_mesh.^2));

            output_plane.fresnel.phaseFactor = exp(1i*SIM_PARAMETERS.k*SIM_PARAMETERS.z)
* ...
                exp(1i*SIM_PARAMETERS.k*(output_plane.x_mesh.^2 +
output_plane.y_mesh.^2)/(2*SIM_PARAMETERS.z));

            output_plane.fresnel.amplitudeFactor = 1/(1i * SIM_PARAMETERS.lambda *
SIM_PARAMETERS.z);

```

```

        output_plane.E =
fftshift(fft2(input_plane.E.*output_plane.fresnel.quadrature));
        output_plane.E = output_plane.E .*output_plane.fresnel.phaseFactor .*
output_plane.fresnel.amplitudeFactor;
        output_plane.I = abs(output_plane.E).^2;

        % Calculate efficiency of grating (relative power of point of interest)
        eff_ratio = getEfficiencyLC_V2(output_plane.I,topologyX_counter,
topologyY_counter);
        result(SIM_PARAMETERS.topologyX_array == topologyX_counter,
SIM_PARAMETERS.topologyY_array == topologyY_counter) = eff_ratio;

        % Calculate angle of diffraction (between 0th and 1st order)
        measuredAngle = getAngleLC(topologyX_counter,topologyY_counter,
output_plane.I, output_plane.axis,SIM_PARAMETERS.z);
        result_ang(SIM_PARAMETERS.topologyX_array == topologyX_counter,
SIM_PARAMETERS.topologyY_array == topologyY_counter) = measuredAngle;
    end
end

%Plotting
if length(SIM_PARAMETERS.topologyX_array) == 1 ||
length(SIM_PARAMETERS.topologyY_array) == 1
    figure
    plot(SIM_PARAMETERS.topologyX_array, result,'o-b')
    title('Diffraction efficiency')
    legend(sprintf('Tp_y = %i', topologyY_counter))
    xlabel('Topology_x (s.n)')
    ylabel('Efficiency (%)')
    grid

    figure
    theoreticalAngle =
rad2deg(asin(SIM_PARAMETERS.lambda./(input_plane.w./SIM_PARAMETERS.topologyX_array)));
%asin(lambda/delta)
    plot(SIM_PARAMETERS.topologyX_array, result_ang);
    hold on
    plot(SIM_PARAMETERS.topologyX_array, theoreticalAngle);
    legend('Simulation', 'Theoretical');
    title(sprintf('Angle deviation\nTp_y = %i', topologyY_counter))
    ylabel('Angle (deg)')
    xlabel('Topology (s.n.)')
    hold off

    figure
    plot(SIM_PARAMETERS.topologyX_array, result_ang-theoreticalAngle')
    title(sprintf('Error at angle calculation\nTp_y = %i', topologyY_counter))
    ylabel('Angle (deg)')
    xlabel('Topology (s.n.)')
else
    figure
    title('Grating efficiency')
    surf(SIM_PARAMETERS.topologyX_array,SIM_PARAMETERS.topologyY_array,result)
    xlabel('Horizontal Topologies')
    ylabel('Vertical Topologies')
    zlabel('Efficiency (%)')

```

```

figure
title('Grating efficiency')
surf(result_ang,result_ang,result)
xlabel('Horizontal Angle (deg)')
ylabel('Vertical Angle (deg)')
zlabel('Efficiency (%)')

figure
surf(SIM_PARAMETERS.topologyX_array,SIM_PARAMETERS.topologyY_array,result_ang)
title('Grating efficiency')
xlabel('Horizontal Topologies (s.n.)')
ylabel('Vertical Topologies (s.n.)')
zlabel('Angle deviation(deg)')

end
else
disp('Choose correctly your method. Ln 67')
end
toc

```

10.4.2. getApertureLC.m

This function will be used to simulate a realistic model from the device that has been designed. The parameters used as input will modify the output model aperture function “modelAF”. “idealAF” is used as a control parameter, and does not take into account any of the input parameters apart from the topology. It will represent a perfect phase distribution for a LC-OPA.

```

function [modelAF, idealAF] = getApertureLC_V2(Topology, nElectrodes, stepsElectrode,
params, Display)
% Obtain the aperture function (rectangular, (x,y)) for a LC cell given
% its phase distribution and the simulation points.
% Params: Topology - Phase distribution
%         nElectrodes - # of cell electrodes
%         stepsElectrodes - # of pixel subdivisions
%         params - Struct with model values
%         Display - Turns on/off graphs about phase an module distribution
% Result: modelAF - Meshgrid of the model discrete field distribution at the
%               aperure
%         idealAF - Meshgrid of the ideal continuous field distribution at the
%               aperure

%-- Initialization
% General Params
tp = abs(Topology); % In case negative, it will be flipped at the end
phase = zeros(nElectrodes,1); % Phase array initialization. Each electrode has an
expected ideal value

% Electrode Params
N = nElectrodes * stepsElectrode; % Matrix size. Commonly 5 electrodes + 1 interpix (6)
AA = ones(N, N); % Phase array
BB = ones(N, N); % Intensity array

pixel_counter = 1; % Pixel being analyzed
actualPhase = 0; % Expected phase in current pixel
nextPhase = 0; % Expected phase in next pixel
previousPhase = 0; % Expected phase in previous pixel

```

```

Q = params.Q; % Set to 1 for all-equal
R1 = params.R1; % 0.5 %Set to 0 for all-equal
FE1=params.FE1; % Fringe Effect electrode D
FE2 = params.FE2; % Fringe Efecct electrode E
FE3 = params.FE3;
QQ= params.QQ; % Interpix intensity percentage
SS = params.SS; % Intensity in the other electrodes

fringeEffect = 'off'; % Enable ('On') or disable ('Off') Fringe effect at subpix D and
E.

%-- Phase generation
% Phase profile
for n = 1:nElectrodes
    a = (2*pi*tp*(n-1))/nElectrodes;
    b = 2*pi;
    phase(n) = rem(a,b); % From 0 to 2pi, tp times
end

n = 1:nElectrodes*stepsElectrode;
a = (2*pi*tp*(n-1))/(nElectrodes*stepsElectrode);
b = 2*pi;
phase_steps(n) = rem(a,b); % From 0 to 2pi, tp times

%-- Plot ideal phase profile
if (strcmp(Display,'On'))
    plot(phase)
    title(sprintf('Ideal phase profile\nTopology %.0f', Topology))
    xlabel('Number of electrode'), xlim([0 nElectrodes])
    ylabel('Phase delay (rad)')
    grid
end

%-- Set disturbance effects. Model for real profile
for electrode_counter = 1:nElectrodes
    actualPhase = phase(electrode_counter);
    if(electrode_counter < nElectrodes)
        nextPhase = phase(electrode_counter + 1);
    else nextPhase = 0;
    end

%-- Interpix and first pix
if electrode_counter == 1 % Case 1st electrode
    % As there is no previous phase, the effect of it is cancelled
    AA(pixel_counter,:) = R1*(actualPhase) + (1-R1)*0; % Interpix
    AA(pixel_counter+1,:) = Q*(actualPhase) + (1-Q)*0; % Subpix A

    BB(pixel_counter,:)= QQ; % Interpix
    BB(pixel_counter+1,:)= SS; % Subpix A

else % Case any other electrode

```

```

previousPhase = phase(electrode_counter - 1);

AA(pixel_counter,:) = R1*(actualPhase) + (1-R1)*(previousPhase); % Interpix
AA(pixel_counter+1,:) = (actualPhase)*Q + (1-Q)*(previousPhase); % Subpix A

BB(pixel_counter,:)=QQ; %interpixel
BB(pixel_counter+1,:)=SS;%pixel A

end

%-- Pix intermediate
intermediateSteps = stepsElectrode-3;
for counter = 1:intermediateSteps
    AA(pixel_counter+1+counter,:) = actualPhase;
    BB(pixel_counter+1+counter,:) = SS;
end

if(strcmp(fringeEffect,'On'))
    if(nextPhase == 0) % Case when the phase drops from 2pi to 0
        AA(pixel_counter+1+counter-2,:) = (actualPhase*FE1); %
Subpix D
        AA(pixel_counter+1+counter-1,:) = FE2*(actualPhase) + FE3*(nextPhase); %
Subpix E

        BB(pixel_counter+1+counter-2) = 1; % Subpix D
        BB(pixel_counter+1+counter-1) = 1; % Subpix E
    end
end

%-- Last pix
if electrode_counter == nElectrodes % Case last electrode
    % As there is no next phase, the effect of it is cancelled
    AA(pixel_counter+1+counter+1,:) = (actualPhase); % Subpix D
    AA(pixel_counter+1+counter+1,:) = Q*(actualPhase) + (0)*(nextPhase); % Subpix E

    BB(pixel_counter+1+counter+1,:) = SS; % Subpix D
    BB(pixel_counter+1+counter+1,:) = SS; % Subpix E

else
    AA(pixel_counter+1+counter+1,:) = (actualPhase); % Subpix
D
    AA(pixel_counter+1+counter+1,:) = Q*(actualPhase) + (1-Q)*(nextPhase); % Subpix
E

    BB(pixel_counter+1+counter+1,:) = SS; % Subpix D
    BB(pixel_counter+1+counter+1,:) = SS; % Subpix E

end

% Continue with the next electrode
pixel_counter = pixel_counter + stepsElectrode;

end

%-- Results
aF_phase = exp(AA.*1i); % Complex notation
aF_module = BB;

```

```

modelAF = aF_module.*aF_phase;
modelAF = modelAF.';

aux = exp(phase_steps.*1i);
idealAF = zeros(length(aux),length(aux));
for counter = 1:length(aux)
    idealAF(counter,:) = aux;
end

if Topology < 0           % Flip orientation in case of negative topology
    modelAF = flipud(modelAF);
end

%-- Output plot
if (strcmp(Display,'On'))
    figure
    plot(AA(:,1))
    title(sprintf('Output phase profile\nTopology %.0f', Topology))
    set(gca,'XTick',linspace(0,N,145))
    set(gca,'XTickLabel',linspace(0,nElectrodes,145)) % To change x axis. 144 instead of
144*6
    xlabel('Number of electrodes')
    ylabel('Phase delay (rad)')
    grid

    figure
    plot(BB(:,1))
    title(sprintf('Output module profile\nTopology %.0f', Topology))
    set(gca,'XTick',linspace(0,N,5))
    set(gca,'XTickLabel',linspace(0,nElectrodes,5))
    xlabel('Number of electrodes')
    ylabel('Relative intensity (%)')
    grid
end

end

```

10.4.3. gaussianBeam2D.m

Generic function used to simulate a two-dimensional gaussian beam. It will be employed to model the laser beam that reaches the device.

```

function [fxy] = gaussianBeam2D(x,y,x0,y0,sigmaX,sigmaY, Display)
% Elliptical (or circular) Gaussian distribution function.
% Top normalized to 1.
% PARAMS:
% x, y - Space where will be evaluated the function. Need to be grided
% sigmaX, sigmaY - Standard deviations
% x0, y0 - Mean

%-- Algorithm
fxy = 1/(2*pi*sigmaX*sigmaY) * exp(-((x-x0).^2/(2*sigmaX^2)+(y-y0).^2/(2*sigmaY^2)));
fxy = fxy/max(max(fxy));

if(strcmp(Display,'On'))
    surf(x,y,fxy, 'LineStyle', 'none')
    title('Input gaussian beam'), xlabel('x'),

```

```

ylabel('y'), xlabel('Relative power (%)')
end
end

```

10.4.4. getAngleLC.m

Auxiliary function that gives the deflection angle for the 1st order beam. It searches the maximum peak neglecting the 0th order and check its position to give a result in degrees based on the output plane distance.

```

function [measuredAngle] = getAngleLC(tp_x,tp_y, output_intensity, output_axis, z)
% This function picks the 1st order peak and calculates the angle based on
% its position at the image plane and the distance from the origin aperture
tp_x = abs(tp_x);
tp_y = abs(tp_y);

r = sqrt(tp_x^2+tp_y^2);

if r > 3
    k = 15; % Number of points used to calculate the principal beam from center. Each
    dimension = 2k+1
    aux = output_intensity;
    aux(length(output_intensity)/2-
k:length(output_intensity)/2+k,length(output_intensity)/2-
k:length(output_intensity)/2+k) = 0;
    [m,i] = max(aux); % Obtain max point
    [m,i2] = max(m);
else
    %disp('Low topologies may lead to get 0th and 1st order mixed up when selecting the
    maximum')
    aux = output_intensity;
    [m,i] = max(aux); % Obtain max point
    [m,i2] = max(m);
end

measuredAngle = rad2deg(atan(sqrt(output_axis(i(i2))^2+output_axis(i2)^2)/z)); %
atg(x/z)

```

10.4.5. getEfficiencyLC

Auxiliary function use to calculate the efficiency ratio for a specific combination of topologies. The algorithm will integrate the power around the peak of interest (1st order) and compare it with the total power present at the output plane.

The approach followed is based in a radius taken from the 1st order maximum. As the topologies increases the beam widens, by the more distance covered as well as by the ellipticity gained due to the projection of the beam, whose propagation direction is not orthogonal to the output plane. The radius will increase with the topologies to counteract this situation.

The main handicap for this algorithm is the calculation of low topologies. 0th and 1st orders are practically combined and splitting the influence of each one is difficult.

```

function [eff_ratio] = getEfficiencyLC(intensity, tp_x, tp_y)
% Params: intensity - Intensity distribution from LC (at output plane)
%         k - # of pixels, beam radius

```

```

%      Nb - # simulation pixels
% Result: effRatio - Relative power from deviated beam over total power
tp_x = abs(tp_x);
tp_y = abs(tp_y);

r = sqrt(tp_x^2+tp_y^2);

if r >=12
    k = 15; % Number of points used to calculate the principal beam from center. Each
dimension = 2k+1
    %k=20;
    aux = intensity;
    aux(length(intensity)/2-k: length(intensity)/2+k,length(intensity)/2-k :
length(intensity)/2+k) = 0;
    [m,i] = max(aux); % Obtain max point
    [m,i2] = max(m);

elseif r > 3
    k = 15; % Number of points used to calculate the principal beam from center. Each
dimension = 2k+1

    aux = intensity;
    aux(length(intensity)/2-k:length(intensity)/2+k,length(intensity)/2-
k:length(intensity)/2+k) = 0;
    [m,i] = max(aux); % Obtain max point
    [m,i2] = max(m);

elseif r >= 2.5 & r<=3
    k = 12; % Number of points used to calculate the principal beam from center. Each
dimension = 2k+1

    aux = intensity;
    [m,i] = max(aux); % Obtain max point
    [m,i2] = max(m);

elseif r >=2 || r < 2.5
    k = 8; % Number of points used to calculate the principal beam from center. Each
dimension = 2k+1

    aux = intensity;
    [m,i] = max(aux); % Obtain max point
    [m,i2] = max(m);

elseif r ==1
    k = 4; % Number of points used to calculate the principal beam from center. Each
dimension = 2k+1

    aux = intensity;
    [m,i] = max(aux); % Obtain max point
    [m,i2] = max(m);

elseif r == 0
    k = 0; % Number of points used to calculate the principal beam from center. Each
dimension = 2k+1

    aux = intensity;
    [m,i] = max(aux); % Obtain max point
    [m,i2] = max(m);

```

```
end
```

```
peak_power = sum(intensity(i(i2)-k:i(i2)+k,i2-k:i2+k),'A11');
```

```
total_power = sum(intensity,'A11');
```

```
eff_ratio = peak_power/total_power*100;
```

```
end
```

11. Bibliography

Checked July 13, 2021

¹https://es.wikipedia.org/wiki/Pantalla_de_cristal_l%C3%ADquido#/media/Archivo:LCD_layers.svg

² Geday, M. A., Caño-García, M., Otón, J. M., Quintana, X., Adaptive Spiral Diffractive Lenses—Lenses With a Twist. *Adv. Optical Mater.* 2020, 8, 2001199. <https://doi.org/10.1002/adom.202001199>

³ Maune, B., Lončar, M., Witzens, J., Hochberg, M., Baehr-Jones, T., Psaltis, D., Scherer, A., & Qiu, Y. (2004). Liquid-Crystal Electric Tuning of a Photonic Crystal Laser. *Applied Physics Letters*, 85, 360-362.

⁴ <https://www.hallcrest.com/color-change-basics/liquid-crystal-thermometers>

⁵ <https://www.provisioneronline.com/articles/109459-liquid-crystal-forehead-thermometers-now-available-as-part-of-palmer-wahls-fever-alert-line>

⁶ <https://www.gauzy.com/smart-glass-with-pdlc-frequently-asked-questions/>

⁷ William J Hossack, Eirini Theofanidou, Jason Crain, Kevin Heggarty, and Martin Birch, "High-speed holographic optical tweezers using a ferroelectric liquid crystal microdisplay," *Opt. Express* 11, 2053-2059 (2003)

⁸ J. K. Doyle, M. J. R. Heck, J. T. Bovington, J. D. Peters, L. A. Coldren, and J. E. Bowers, "Two-dimensional free-space beam steering with an optical phased array on silicon-on-insulator," *Opt. Express* 19, 21595-21604 (2011)

⁹ Li, C.; Cao, X.; Wu, K.; Li, X.; Chen, J. Lens-Based Integrated 2D Beam-Steering Device with Defocusing Approach and Broadband Pulse Operation for Lidar Application. *Opt. Express* 2019, 27, 32970, doi:10.1364/OE.27.032970.

¹⁰ Lin, Y.; Ai, Y.; Shan, X.; Liu, M. Simulation of Two-Dimensional Target Motion Based on a Liquid Crystal Beam Steering Method. *Opt. Eng.* 2015, 54, 056102, doi:10.1117/1.OE.54.5.056102

¹¹ Hellman, B.; Luo, C.; Chen, G.; Rodriguez, J.; Perkins, C.; Park, J.-H.; Takashima, Y. Single-Chip Holographic Beam Steering for Lidar by a Digital Micromirror Device with Angular and Spatial Hybrid Multiplexing. *Opt. Express* 2020, 28, 21993, doi:10.1364/OE.394114

¹² Paul F. McManamon, Abtin Ataei, "Progress and opportunities in optical beam steering," *Proc. SPIE 10926, Quantum Sensing and Nano Electronics and Photonics XVI*, 1092610 (29 May 2019); <https://doi.org/10.1117/12.2511987>

¹³ <https://www.newport.com.cn/p/FSM-300-01>

¹⁴ <https://www.aerotech.com/wp-content/uploads/2021/01/amg-gr.pdf>

¹⁵ Yang, J.; Su, X.; Xu, P.; Gu, Z. Beam Steering and Deflecting Device Using Step-Based Micro-Blazed Grating. *Opt. Commun.* 2008, 281, 3969–3976, doi:10.1016/j.optcom.2008.04.032

¹⁶ Otón, E.; Pérez-Fernández, J.; López-Molina, D.; Quintana, X.; Otón, J.M.; Geday, M.A. Reliability of Liquid Crystals in Space Photonics. *IEEE Photonics J.* 2015, 7, 1–9, doi:10.1109/JPHOT.2015.2451626

-
- ¹⁷ He, Z.; Gou, F.; Chen, R.; Yin, K.; Zhan, T.; Wu, S.-T. Liquid Crystal Beam Steering Devices: Principles, Recent Advances, and Future Developments. *Crystals* 2019, 9, 292. <https://doi.org/10.3390/cryst9060292>
- ¹⁸ Kim, Y.; Won, K.; An, J.; Hong, J.-Y.; Kim, Y.; Choi, C.-S.; Song, H.; Song, B.; Suk Kim, H.; Bae, K.-D.; et al. Large-Area Liquid Crystal Beam Deflector with Wide Steering Angle. *Appl. Opt.* 2020, 59, 7462, doi:10.1364/AO.398863.
- ¹⁹ <https://en.wikipedia.org/wiki/Birefringence>
- ²⁰ Peatross, J., & Ware, M. (2015). *Physics of light and optics*. Brigham Young University, Department of Physics., p.124
- ²¹ Peatross, J., & Ware, M. (2015). *Physics of light and optics*. Brigham Young University, Department of Physics, p.128
- ²² Farnell, James. (2010). Nonlinear and Tunable Metamaterials. 10.13140/RG.2.2.21719.93608.
- ²³ <http://www.lc-science.info/lcscience/the-nematic-phase/>
- ²⁴ <https://nl.wikipedia.org/wiki/Fresnellens>
- ²⁵ Mcmanamon, Paul & Dorschner, T.A. & Corkum, D.L. & Friedman, L.J. & Hobbs, D.S. & Holz, Mathias & Liberman, S. & Nguyen, H.Q. & Resler, Daniel & Sharp, R.C. & Watson, Edward. (1996). Optical phased array technology. *Proceedings of the IEEE*. 84. 268 - 298. 10.1109/5.482231.
- ²⁶ Wang, X.; Wu, L.; Li, M.; Wu, S.; Shang, J.; Qiu, Q. Theoretical and Experimental Demonstration on Grating Lobes of Liquid Crystal Optical Phased Array. *Int. J. Opt.* 2016, 2016, 1–6.
- ²⁷ Otón, J.M.; Otón, E.; Quintana, X.; Geday, M.A. Liquid-Crystal Phase-Only Devices. *J. Mol. Liq.* 2018, 267, 469–483, doi:10.1016/j.molliq.2017.10.148.
- ²⁸ Bennis, N.; Geday, M.; Quintana, X.; Cerrolaza, B.; Medialdea, D.; Spadło, A.; Dąbrowski, R.; Otón, J. Nearly-Analogue Blazed Phase Grating Using High Birefringence Liquid Crystal. *Opto Electron. Rev.* 2009, 17, doi:10.2478/s11772-008-0074-4.
- ²⁹ Blas, Mario & Geday, Morten & Otón, José & Quintana, Xabier. (2021). Two-Dimensional Digital Beam Steering Based on Liquid Crystal Phase Gratings. *Applied Sciences*. 11. 3632. 10.3390/app11083632.
- ³⁰ Tunable organic waveguides and microstructured devices – Manuel Caño-García
- ³¹ <https://www.europages.co.uk/UVOCleaner/JELIGHT-COMPANY/cpid-5385996.html>
- ³² Yamahara, Motohiro & Nakamura, Mariko & Koide, Naoyuki & Sasaki, Takeo. (2007). Influence of rubbing conditions of polyimide alignment layer on optical anisotropy of immobilized liquid crystal film. *Liquid Crystals - LIQ CRYST.* 34. 381-387. 10.1080/02678290601097334.
- ³³ Jones L.P. (2012) Alignment Properties of Liquid Crystals. In: Chen J., Cranton W., Fihn M. (eds) *Handbook of Visual Display Technology*. Springer, Berlin, Heidelberg. https://doi.org/10.1007/978-3-540-79567-4_86
- ³⁴ Manuel Caño-García, Ahmed Elmogi, Marie-Aline Mattelin, Jeroen Missinne, Morten A. Geday, José M. Otón, Geert Van Steenberge, and Xabier Quintana, "All-organic switching polarizer based on polymer waveguides and liquid crystals," *Opt. Express* 26, 9584-9594 (2018)
- ³⁵ Goodman, J. W. (1996). *Introduction to Fourier optics*. New York: McGraw-Hill.
- ³⁶ Hecht, E. (2017). *Diffraction*. In *Optics* (4th ed.). chapter, Addison Wesley.